JOURNAL OF GEOPHYSICAL RESEARCH, VOL. 106, NO. E12, PAGES 33,053–33,078, DECEMBER 25, 2001

Io in the near infrared: Near-Infrared Mapping Spectrometer (NIMS) results from the Galileo flybys in 1999 and 2000

Rosaly M. C. Lopes,[1] L. W. Kamp,[1] S. Douté,[2] W. D. Smythe,[1] R. W. Carlson,[1] A. S. McEwen,[3] P. E. Geissler,[3] S. W. Kieffer,[4] F. E. Leader,[5] A. G. Davies,[1] E. Barbinis,[1] R. Mehlman,[5] M. Segura,[1] J. Shirley,[1] and L. A. Soderblom[6]

Abstract. Galileo's Near-Infrared Mapping Spectrometer (NIMS) observed Io during the spacecraft's three flybys in October 1999, November 1999, and February 2000. The observations, which are summarized here, were used to map the detailed thermal structure of active volcanic regions and the surface distribution of SO_2 and to investigate the origin of a yet unidentified compound showing an absorption feature at ~1 μm. We present a summary of the observations and results, focusing on the distribution of thermal emission and of SO_2 deposits. We find high eruption temperatures, consistent with ultramafic volcanism, at Pele. Such temperatures may be present at other hot spots, but the hottest areas may be too small for those temperatures to be detected at the spatial resolution of our observations. Loki is the site of frequent eruptions, and the low thermal emission may represent lavas cooling on the caldera's surface or the cooling crust of a lava lake. High-resolution spectral observations of Emakong caldera show thermal emission and SO_2 within the same pixels, implying that patches of SO_2 frost and patches of cooling lavas or sulfur flows are present within a few kilometers from one another. Thermal maps of Prometheus and Amirani show that these two hot spots are characterized by long lava flows. The thermal profiles of flows at both locations are consistent with insulated flows, with the Amirani flow field having more breakouts of fresh lava along its length. Prometheus and Amirani each show a white ring at visible wavelengths, while SO_2 distribution maps show that the highest concentration of SO_2 in both ring deposits lies outside the white portion. Visible measurements at high phase angles show that the white deposit around Prometheus extends into the SO_2 ring. This suggests that the deposits are thin and that compositional or grain size variations may occur in the radial direction. SO_2 mapping of the Chaac region shows that the interior of a caldera adjacent to Chaac has almost pure SO_2. The deposit appears to be topographically controlled, suggesting a possible origin by liquid flow.

1. Introduction

Io is the only place outside the Earth where large-scale active volcanism has been observed. The dynamic nature of Io's volcanism makes temporal studies particularly important, and such studies have been made using both spacecraft data and ground-based observations. One of the major objectives of the Galileo mission was to acquire high spatial resolution coverage of Io in the visible and infrared. These observations were obtained during three flybys of Io in October 1999 (orbit I24), November 1999 (orbit I25), and February 2000 (orbit I27). Prior to these flybys, it was known that Io's surface is dotted with active hot spots [*Lopes-Gautier et al.*, 1997; *McEwen et al.*, 1997, 1998a; *Lopes-Gautier et al.*, 1999; *Marchis et al.*, 2000] and covered by SO_2 frost and other compounds [*Carlson et al.*, 1997; *Geissler et al.*, 1999; *Douté et al.*, 2001a]. It was postulated that volcanic plumes, which are present at some hot spots, inject gaseous SO_2 into the atmosphere. The gaseous SO_2 diffuses and condenses as frost on the surface. The frost deposits serve as tracers that are useful for studying volcanic control over surface evolution. The hot spots, many of which are persistently active [*Lopes-Gautier et al.*, 1999; *Lopes-Gautier*, 1999], are surface expressions of the tidal heating that provides the energy for Io's active volcanism.

Io's volcanic activity and SO_2 distribution have been studied using data acquired by the near-infrared mapping spectrometer (NIMS) since June 1996. Observations prior to the flybys were obtained with spatial resolutions ranging from 65 km/NIMS pixel (for one observation in orbit C21) to over 500 km/NIMS pixel. These distant observations (111 in total) allowed us to make global studies of the distribution and temporal variations of volcanic activity [*Lopes-Gautier et al.*, 1997, 1999] and to map the SO_2 frost and obtain insights about its cycle [*Carlson et al.*, 1997; *Douté et al.*, 2001a]. Joint studies with Galileo's solid-state imaging system (SSI) were used to detect high-temperature volcanism [*McEwen et al.*, 1998b; *Davies et al.*, this issue] and to study the correlation of thermal

[1]Jet Propulsion Laboratory, California Institute of Technology, Pasadena, California.
[2]Laboratoire de Planetologie de Grenoble, CNRS, Grenoble, France.
[3]Lunar and Planetary Laboratory, University of Arizona, Tucson, Arizona.
[4]S. W. Kieffer Science Consulting, Inc., Bolton, Ontario, Canada.
[5]Institute for Geophysics and Planetary Physics, University of California, Los Angeles, California.
[6]U.S. Geological Survey, Flagstaff, Arizona.

Paper number 2000JE001463.
0148-0227/01/2000JE001463$09.00

emission detected by NIMS with surface colors and plumes [*Lopes-Gautier et al.*, 1999; *Geissler et al.*, 1999]. However, the relatively low spatial resolution of the distant observations did not permit local-scale, detailed studies of particular volcanic regions to be made.

Galileo's three flybys of Io provided an unprecedented opportunity to study specific volcanic regions at high spatial resolution, thus examining the role of volcanism at local rather than global scales. Preliminary results were reported by *Lopes-Gautier et al.* [2000a]. This paper summarizes the NIMS observations and the results of our further analyses, focusing on thermal mapping and new data from the I27 orbit.

2. Observations

The NIMS instrument has been described by *Carlson et al.* [1992] and *Smythe et al.* [1995]. NIMS includes a spectrometer with a scanning grating and spans the wavelength range 0.7 to 5.2 μm, therefore measuring both reflected sunlight and thermal emission. NIMS forms spectra with 17 detectors in combination with the moving grating. The 17 wavelengths (spaced across the wavelength range) obtained for each grating position are acquired simultaneously. During the Galileo main mission and the Galileo Europa mission (GEM), two of the NIMS detectors (3 and 8) stopped working, and the sensitivity of the first two detectors was considerably reduced. Prior to the first NIMS observation in I24, grating motion ceased, probably from radiation damage to the electronics. The grating is stopped at the short-wavelength end of the scan. Recovery has not been successful so far.

Because of the stopped grating, the observations during the Io flybys obtained 13 fixed infrared (IR) wavelengths (in the range from 1.0 to 4.7 μm) instead of the planned 360 (Figure 1). However, this anomalous operation provided greater sampling frequency (24 samples instead of 1) at each wavelength, increasing the signal/noise ratio substantially and mitigating the problem of radiation spikes in the data. The reduced number of wavelengths is suitable for temperature determination and band ratio mapping (for SO_2 and the absorption band in the 1-μm region), but our search for yet unknown surface compounds was compromised. SO_2 band ratio mapping for specific regions was reported by *Lopes-Gautier et al.* [2000a]. Modeling to relate the band ratio mapping from the flyby observations to results obtained from the full NIMS spectral range is being done by *Douté et al.* [2000].

The NIMS observations are listed in Table 1. NIMS obtained 17 observations during I24, 4 observations during I25, and 10 observations during I27. Additional observations, at reduced spatial sampling, were obtained while SSI acquired data. These are listed in Table 1 as "ride-along observations." Spatial resolution ranged from 0.5 to 25 km/NIMS pixel for most observations. The gain state (GS) was set at nominal (GS 2) for dayside observations, twice the nominal gain (GS 3) for observations near the terminator, and 4 times the nominal gain (GS 4) for nightside observations. Because the nightside observations of active volcanic regions during I24 and I25 showed saturation, GS 2 was used for nightside observations during I27. In the case of Pele, considerable saturation was still present, particularly at wavelengths in the middle of the NIMS range.

The observations targeted volcanic regions of diverse types. Nearly every observation was collaborative with SSI, so that both instruments observed the same target almost simultaneously. The SSI observations are described by *Keszthelyi et al.* [this issue]. NIMS data were navigated onto SSI images whenever possible, so that correlations could be made between features and colors seen in the visible images and thermal output and spectral ratio maps obtained from NIMS data. The NIMS data have not all been analyzed in detail. Here we add to the preliminary results reported by *Lopes-Gautier et al.* [2000a] and focus on the analysis of data from I27.

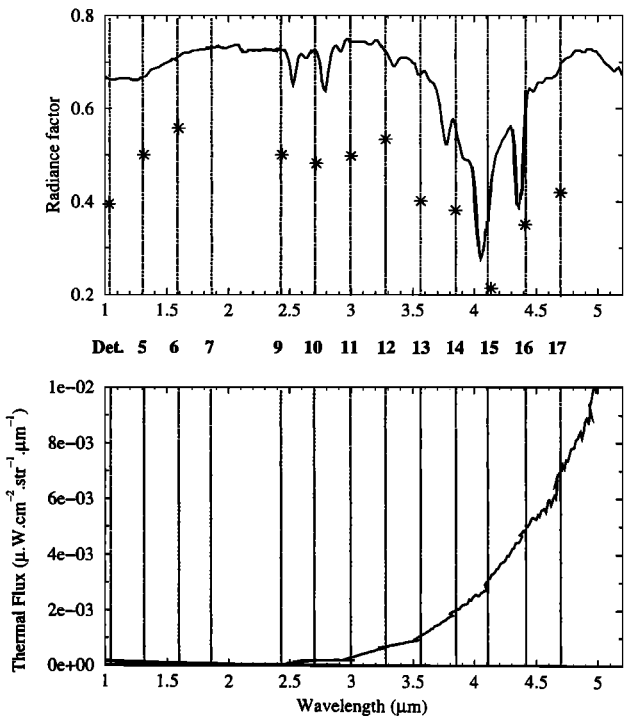

Figure 1. NIMS spectra showing wavelengths obtained during the flyby observations, compared to NIMS spectra showing wavelengths available prior to the grating becoming stuck. The horizontal scale gives wavelength and the corresponding NIMS detectors. (top) NIMS spectrum of Io in reflected sunlight (solid line) obtained from a global observation taken in September 1996 (orbit G2). The spectrum (a regional average) shows SO_2 absorptions and is described by *Carlson et al.* [1997]. Vertical lines show the wavelengths obtained during I24 and I25, after the instrument's scanning grating malfunctioned. Stars show a typical spectrum obtained during I24 with this reduced number of wavelengths (the difference between the radiance factors for these spectra is due to different illumination angles). Detector 7 has not given a reliable signal since the grating malfunctioned and hence is not shown in this spectrum. SO_2 mapping was done using a ratio of detector 12 (3.28 μm) to detector 15 (4.13 μm) radiances. (bottom) NIMS spectrum over the Isum hot spot, with the reflected sunlight contribution removed (method explained by *Soderblom et al.* [1999]). This spectrum was obtained from the same global observation (in orbit G2) as the spectrum shown above. The reduced number of wavelengths in I24 (shown by the dotted vertical lines) is sufficient for obtaining a single-temperature thermal fit to the data.

3. SO_2 Mapping

For SO_2 band ratio mapping, we used the 4.1-μm spectral channel, which lies within the strong SO_2 $\nu_1 + \nu_3$ absorption band (Figure 1). We use the radiance values at 4.13 μm rela-

Table 1. NIMS Observations From the Galileo Flybys in Orbits I24, I25, and I27

Observation	Target	Gain State	Resolution, km/NIMS pixel	Size, km	Detections/Comments
			NIMS Observations in I24		
24INLOKIRA01	Loki, nightside	GS 4	1.3–2.1	45 × 18[a]	Loki "island" and caldera floor/temperatures maps show color temperatures <350 K
24INHSPELE01	Pele, nightside	GS 4	1.0	15 × 1.3	hot spot detected at (−18.5°, 255.6°W)
24INPILLAN01*	Pillan, near terminator	GS 4	0.5		data obtained as "ride-along" with SSI, meaning few samples collected
24INPILLAN01	Pillan, near terminator	GS 4	0.5	7 × 1	hot spot detected at (−10.5°, 241.8°W)
24INCOLCHS01	Colchis Regio region, centered at +3.6°, 214.1°W, dayside	GS 2	0.4	22 × 61[b]	bright white region, no hot spot/problem with target motion compensation (TMC) led to partial coverage
24INZAMAMA01	Zamama hot spot, dayside	GS 2	1.0	88 × 104[b]	missed hot spot at +18°, 173°W, but detected thermal emission at +17.9°, 170.4°W)/problem with target motion compensation (TMC) led to partial coverage
24INPROMTH01*	Prometheus flow, dayside	GS 2			data obtained as "ride-along" with SSI, meaning few samples collected/data show thermal emission along length of flow
24INPROMTH01	Prometheus, dayside	GS 2	1.8	70 × 14	hot spot at −1.7°, 155°W
T24INCOLCHS02	Colchis Regio region, near Mulungu, dayside	GS 2	4.5	92 × 14	no hot spot, little apparent spectral variation
24INNTOHIL01	Tohil (no hot spot but red areas)	GS 2	5.0	112 × 13	red deposits show enhanced SO_2 concentration
24INPROMTHS02	Prometheus, dayside	GS 2	5.5–8.5	186 × 80	two major hot spots detected, thermal emission detected along length of lava flow
24INZAMAMA02*	Zamama, dayside	GS 2			data obtained as "ride-along" with SSI, meaning few samples collected
24INZAMAMA02	Zamama, dayside	GS 2	9.5	234 × 46	hot spot (flow) detected
24INDORIAN01	golf course, dayside	GS 2	11.0	253 × 28	missed area of bright green deposits due to targeting uncertainty
24INAMSKGI01*	Amirani flow, dayside	GS 2			data obtained as "ride-along" with SSI, meaning few samples collected
24INAMSKGI01	Amirani flow, dayside	GS 2	12.0	306 × 85	three major hot spots detected along flow/SO_2 analysis shows positive correlation with red deposits
24INTERMAP01	region near terminator	GS 3	14.0	319 × 28	a few pixels show weak thermal emission
24INREGION01	Prometheus region	GS 2	22.0–25.0	972 × 168	Prometheus fallout ring from SO_2 plume detected/thermal emission detected from eight main locations: Prometheus (two adjacent areas), Culann (two adjacent areas), Tupan, Camaxtli, (+14°, 150°W), (+22°, 146°W), (+15°, 139°W), and (+12°, 134°W)
24INPPLUME01	Pillan plume, dayside	GS 4	32.0	surface and off limb	plume not detected/Pillan hot spot detected on limb
24INPELEPM01	Pele plume, dayside	GS 4	52.0	surface and off limb	plume not detected/thermal emission from Marduk and Reiden detected (first detection of Reiden since G1)
24INREGION02	nearly global	GS 2	105	nearly global	thermal emission detected from 13 main locations: Culann, Tupan, Malik, Prometheus (two adjacent areas), Zamama, Itzamna, Isum (two adjacent areas), Marduk, Pillan, Pele, Gabija, Ot, and (+22°, 146°W)/Prometheus fallout ring from SO_2 plume detected
24INGLOCOL01*	global mosaic, dayside	GS 2			data obtained as "ride-along" with SSI, meaning few samples collected

Table 1. (continued)

Observation	Target	Gain State	Resolution, km/NIMS pixel	Detections/Comments
		NIMS Observations in I25		
INGIANTS01	Tvashtar Catena	GS 3	9.2	very bright hot spot, fire fountain eruption detected by SSI and from ground/minimum temperature from NIMS of 1120 K
INCULANN01	Culann hot spot, dayside	GS 2	11	positive correlation between SO_2 and red deposits
ININTERM01	Gish Bar	GS 3	13	thermal emission detected from Gish Bar (two adjacent areas)
INREGION01	Prometheus region, dayside	GS 2	14–25	Prometheus region; Prometheus SO_2 fallout ring detected; thermal emission detected at 5 main locations: Prometheus (two adjacent areas), Chaac, (−5°, 132°W), (−2°, 144°W), and (+9.5°, 132°W)/first detection of a hot spot at Chaac
		NIMS Observations in I27		
27INHRPELE01	Pele, nightside	GS 2	1–1.9	mosaic of Pele hot spot
27INPELE_01*	Pele, nightside	GS 2	0.85–0.9	data obtained as "ride-along" with SSI, meaning few samples collected
27INPROMTH01*B	Prometheus, dayside	GS 2	0.6–0.7	data obtained as "ride-along" with SSI, meaning few samples collected
27INICHAAC01	Chaac, dayside	GS 2	0.9–1.4	short mosaic of Chaac hot spot
27INMOSAIC01	Chaac region, dayside	GS 2	1.7–5.3	Chaac, part of the caldera (not hot spot) and nearby caldera to the east where SO_2 abundance is very high
27INPROMTH01	Prometheus, dayside	GS 2	6–7.5	mosaic of Prometheus flow and inner SO_2 ring
27INTOHIL_01*	Tohil, dayside	GS 2	8	data obtained as "ride-along" with SSI, meaning few samples collected
27INPROMTH02*	Prometheus, dayside	GS 2	8.5	data obtained as "ride-along" with SSI, meaning few samples collected
27INCAMAXT01	Camaxtli, dayside	GS 2	9–10	NIMS mosaic of Camaxtli hot spot plus SSI ride-along data west of Camaxtli, including Chaac; thermal emission detected from Camaxtli (two adjacent areas), Chaac, (+14°, 150°W), (+15°, 139°W), and (+12°, 134°W)
27INAMIRANI01	Amirani flow, dayside	GS 2	10.5–15	mosaic of Amirani flow and SO_2 plume deposit; SO_2 fallout ring from plume detected; thermal emission detected all along main flow (oriented N–S) but not from western flow; thermal emission detected from dark caldera southwest of the flow
27INTVASHT01*B	Tvashtar, dayside	GS 2	15.5	data obtained as "ride-along" with SSI, meaning few samples collected
27INZALTRM01*	Zal, dayside	GS 2	16.5	data obtained as "ride-along" with SSI, meaning few samples collected; thermal emission detected from Zal hot spot; thermal emission also detected at edge of observation at (+36.5°, 88°W)/position of this previously unidentified hot spot could not be determined accurately as not enough area was covered by NIMS
27INTVASHT01B	Tvashtar	GS 2	18.5	NIMS mosaic of eastern part of Tvashtar
27INREGION01	Prometheus region	GS 2	20–29.5	Prometheus region; Prometheus SO_2 fallout ring detected; thermal emission detected from 15 main locations: Prometheus (two adjacent areas), Tupan, Camaxtli, Emakong, (+22°, 152°W), (+22°, 146°W), (+14°, 150°W), (0, 164°W), (−5°, 132°W), (+9.5°, 132°W), (+12°, 134°W), (+15°, 139°W), (+20°, 131°W), and (+16.5°, 124°W)
27INGLOBAL01	part global coverage	GS 2	80.5–87.5	strong thermal emission detected from Tvashtar; nine other hot spots detected but significant "wobble" in observation makes identification of hot spots difficult, as accurate positions could not yet be obtained

[a]Plus data as platform scanned to Pele.
[b]Partial coverage.

tive to the radiances at a nonabsorbing wavelength (3.28 μm) as a measure of the amount of SO_2 absorption. The spectral ratio is defined as the ratio $[A(3.28)/A(4.13)]$, where $A(\lambda)$ is the measured albedo (bidirectional reflectance) at wavelength λ μm. Pixels in which significant thermal emission is present ($T_B > 200$ K, see section 4) do not show the absorption at 4.13 μm (except in the case of Emakong, discussed in section 4.3); hence for these pixels the ratio is close to zero. We did not take photometric variations into account, as the phase angle does not change significantly during the acquisition of the high-resolution observations used in the mapping, and comparisons are not made between observations at different phase angles.

This ratio is a qualitative SO_2 indicator, as discussed by *Lopes-Gautier et al.* [2000a], because the spectral ratio depends on the SO_2 abundance, the mean grain size, and the presence of other materials and their mixing mode (spatially segregated or intimately mixed at the scale of photon path lengths). Work is in progress to actually invert both a macroscopic and an intimate mixing model using two spectral ratios $[A(3.28)/A(4.13)]$ and $[A(3.28)/A(3.56)]$. Such analysis leads to quantitative values for SO_2 abundance and mean grain size with reasonable accuracy [*Douté et al.*, 2000]. In this paper, we assume a spatially segregated mixing with spectrally flat material, which gives upper bounds to the SO_2 abundance. The depth of sampling at 4.13 μm is limited to ~1 mm, so we cannot distinguish between thick frost deposits and thin layers (that can be transparent in the visible and at nonabsorbing IR wavelengths).

3.1. Background

Preliminary results on the distribution of SO_2 at local scales applying this method to data from I24 and I25 were presented by *Lopes-Gautier et al.* [2000a]. This earlier analysis used a different wavelength as the nonabsorbing wavelength (3.00 μm). In the current work, we used 3.28 μm because we have found it to be less susceptible to random noise, though the overall results do not change significantly. Our earlier maps [*Lopes-Gautier et al.*, 2000a] were obtained from observations of the Prometheus region and Culann Patera. The SO_2 ratio map of the Prometheus area showed a striking SO_2 deposition ring circling the present plume vent. When compared with low-phase visible images, this ring appeared larger than its visible white counterpart. However, *Geissler et al.* [this issue] have shown that visible images obtained at low phase angles are insensitive to thin, nonabsorbing frost deposits. Geissler et al. proposed that areas of Io that appear unexpectedly bright at high phase angles are covered by fine-grained SO_2 frosts that are too thin to be seen in visible wavelengths under normal illumination. These frosts correspond to the areas rich in SO_2 frosts identified from earlier high-resolution mapping from NIMS data [*Douté et al.*, 2000; *Lopes-Gautier et al.*, 2000a]. Visible images of Prometheus obtained at a high phase angle give shapes and dimensions of the ring that are consistent with the SO_2-rich ring seen in NIMS data.

NIMS SO_2 determinations and high-phase SSI measurements correlate well at local scales and, to a lesser extent, at global scales [*Geissler et al.*, this issue], but comparisons of SO_2 maps with SSI-derived color maps show only some small-scale correlations. For example, the SO_2 ratio maps of Culann Patera and Tohil Patera showed locally enhanced concentrations of SO_2 that coincided with deposits having a pink to red appearance at visible wavelengths [*Lopes-Gautier et al.*, 2000a, Figure 4]. However, in the case of an area east of Prometheus, red deposits are found within and beyond the SO_2-rich ring, but there is no local enhancement of SO_2 in the red-colored deposits. Red deposits on Io are thought to be short-chain sulfur allotropes S_x (x = 2, 3, 4, 6) [*Spencer et al.*, 1997]. Their occasional association with SO_2 at small scales suggests a deposition or emission process that prevents the spatial segregation of S and SO_2, even though these compounds have different volatilities. Two possibilities were suggested by *Lopes-Gautier et al.* [2000a]. In one case, a relatively high S_2/SO_2 ratio can lead to a dense atmospheric population of radiatively cooled S_2 solid nuclei on which SO_2 could condense. Another possibility is that boiling liquid SO_2 with short-chain S or other coloring agents dissolved in it may reach the surface from below and freeze before complete sublimation. Radiolysis of SO_2 and sulfur may also produce short chain allotropes. The presence of both SO_2 and S_2 in a single plume has been detected by *Spencer et al.* [2000] at Pele. Spencer et al. suggested that simple cocondensation of the two gases could result in an intimate mixture in which the less abundant but darker S_2 could dominate the visible spectrum.

3.2. Current Analysis

Our current analysis of SO_2 distribution uses observations from I27 of the Amirani and Chaac regions. We also use a SSI high-resolution image of Culann from I25 to test the correlation presented by *Lopes-Gautier et al.* [2000a], and we present the SO_2 distribution map of Tohil from I24 which was not shown in our previous work.

3.2.1. Amirani. The SO_2 ratio map for the Amirani region (from 27INAMIRANI01) shows the distribution of SO_2 around the flow and caldera (Plate 1). The map shows several notable features. The first is the presence of an anticorrelation between SO_2 spectral ratio and the low-albedo flow to the west of the main Amirani flow, from which no significant thermal emission can be detected by NIMS (see section 4.2). Low-albedo areas on Io are often hot (for example, the Amirani caldera and the main north-south lava flow) and therefore often must be excluded from our SO_2 band ratio maps, as explained above. The low-albedo western Amirani flow is one of the few low-albedo areas imaged by NIMS at high spatial resolution that does not show significant thermal emission. It appears to be an older, cooled lava flow. The flow leads to the location of the Maui plume imaged by Voyager (this location was not covered by the NIMS observation). Galileo has not detected a plume at Maui and the plume may have been driven by the lava flow [*McEwen et al.*, 1998a], perhaps in a way similar to the Prometheus plume. The cessation of flow activity may therefore have led to that of the plume.

Another feature shown by the map is a relatively low SO_2 band ratio over the bright white area that appears to form a ring around the southern part of the Amirani main (north-south) lava flow. This lack of a positive correlation between bright white deposits and SO_2 concentration agrees with our other results for Prometheus described by *Lopes-Gautier et al.* [2000a]. The white ring-like deposit on Amirani is interpreted from the visible images as a plume deposit [*Keszthelyi et al.*, this issue], but it is not clear from the images where the plume vent is. The SO_2 ratio map shows that this white plume deposit does not correspond to the main area of SO_2 deposition but shows that SO_2 is more abundant in areas farther out from the plume vent and may form a second ring. The NIMS observation does not cover a sufficiently large area to be able to confirm the

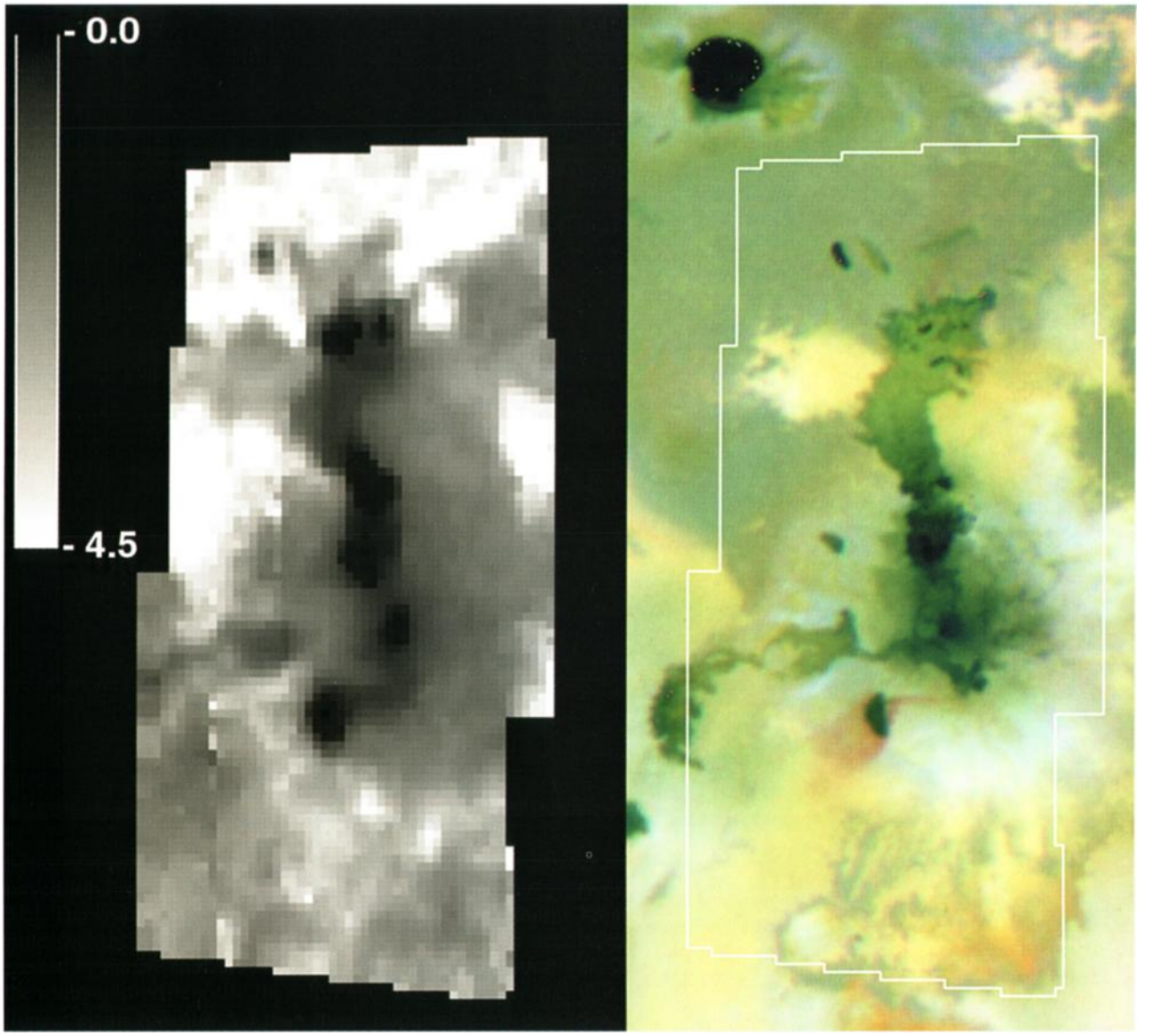

Plate 1. Amirani lava flow imaged by NIMS during I24 and I27. (left) A NIMS band ratio map showing relative SO_2 concentration, made from the I27 data. Higher values of the ratio (up to 4.5 on the sidebar scale) represent enhanced concentration of SO_2. (right) Image obtained by SSI during orbit C21, with the area covered by NIMS delineated. The NIMS band ratio map shows that deeper band depths of SO_2 (bright) do not coincide with the visible white ring in the SSI image. The dark pixels corresponding to the area of the active flow (trending north-south) contain significant thermal emission; thus the value of the band ratio is close to zero and these pixels appear dark. SO_2 is depleted (dark) over the flow that runs toward the west, but this flow is not active at present. A general gradient for the band ratio can be seen from south to north, with SO_2 being enhanced toward the greenish terrain to the north. This may indicate possible gas transport from Amirani to higher latitudes. SO_2 appears less abundant on the yellow terrain south and east of the flow and on a patch to the northwest of the flow. It is also possible that the yellow terrain may represent a deposit containing non-SO_2 compounds that is overlying the greenish materials.

presence of a second, outward ring that is richer in SO_2, as was observed for Prometheus from I24 data [*Lopes-Gautier et al.*, 2000a]. The visible white ring at Amirani may contain another volatile such as sulfur or, possibly, anhydrous salts such as suggested by *Fanale et al.* [1974]. However, if sulfur is present in the white-colored deposits, the sulfur allotropes are likely to be longer chain (possibly S_8) than those responsible for the orange/red deposits such as present around Pele [*Spencer et al.*, 2000].

The eruptive styles at Amirani and Prometheus may be similar, as discussed in the thermal analysis section below and by *Keszthelyi et al.* [this issue] and *Davies et al.* [2000a]. Furthermore, Prometheus and Amirani are sites of long-lived plumes that may be caused by the interaction of hot lava with SO_2 frost [*Kieffer et al.*, 2000; *Milazzo et al.*, this issue]. The NIMS data indicate that plumes at both sites may be producing compounds other than SO_2, such as sulfur molecules, that condense closer to the plume vent than SO_2 and form the white deposits. However, the plume deposit at Prometheus is considerably more sharply defined in both the visible and infrared wavelengths.

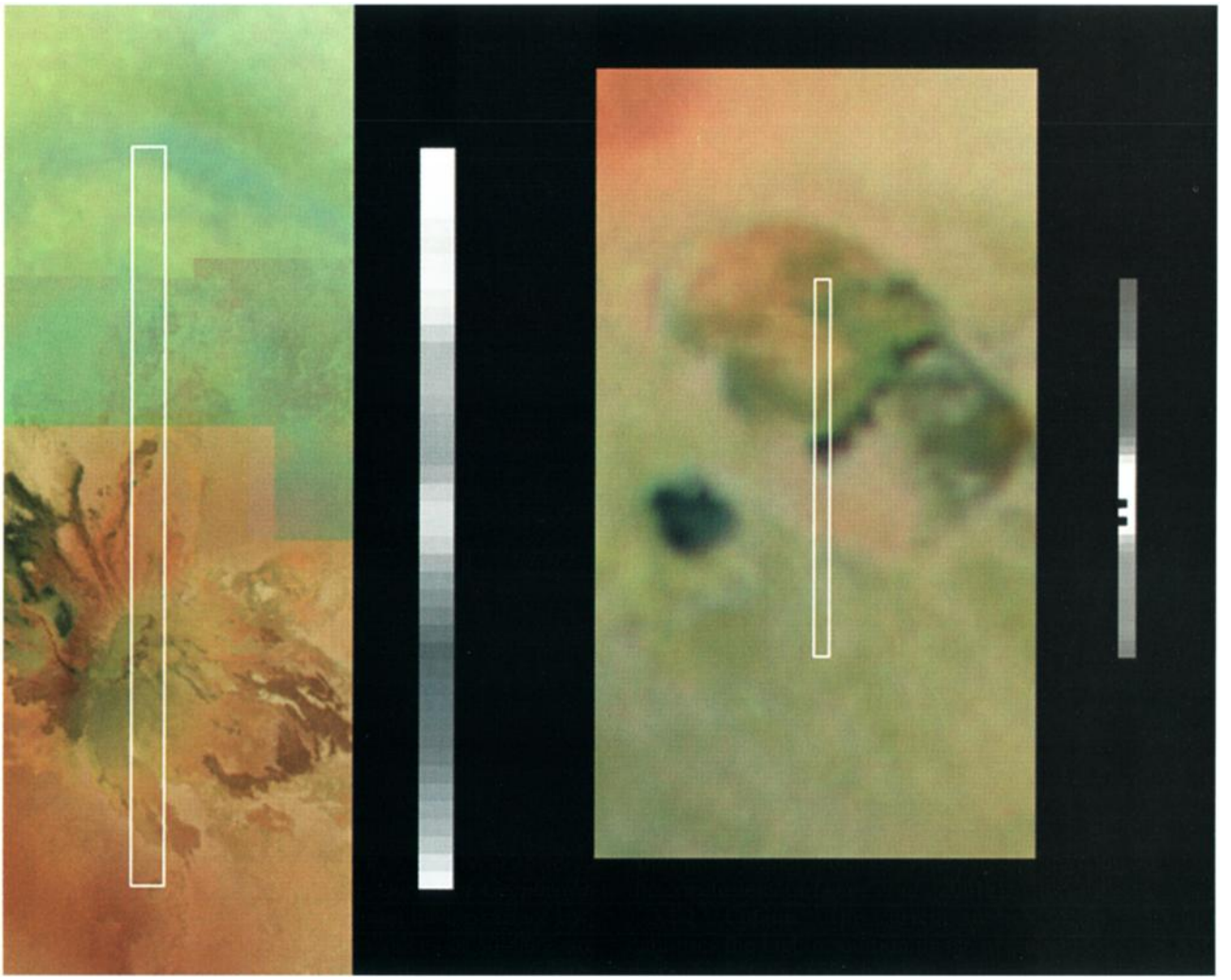

Plate 2. (left) Culann hot spot as observed by NIMS and SSI during I25 and (right) Tohil Patera, which is not an active hot spot, observed by NIMS during I24. In both observations, NIMS obtained a narrow strip of data from which a band ratio map showing relative SO_2 concentration was obtained. The background images are from SSI, showing visible colors, with the area covered by the NIMS data delineated. In the case of Tohil the SSI image is from orbit C21. For Culann, high-resolution imaging is available from orbit I25 (the northern part is a lower-resolution image from orbit C21). The NIMS band ratio maps are shown to the right of each image. Enhanced concentrations of SO_2 (bright) are seen over areas that are pink to red in visible wavelengths for both Tohil and Culann. The relative concentration of SO_2 is low (dark) near the Culann caldera, which has a greenish color. The spatial resolution of NIMS is 11 km/pixel for Culann and 5 km/pixel for Tohil.

Another significant difference between the SO_2 distribution around Prometheus and Amirani is that the Amirani region is richer in SO_2. Using a linear-mixing model, *Douté et al.* [2001b, also Dynamics and evolution of SO_2 gas condensation around Prometheus-like plumes on Io as seen by the Near-Infrared Mapping Spectrometer, submitted to *Journal of Geophysical Research*, 2001] find areas around Amirani having surface coverage of 80–100%, whereas maximum values of 80–90% are observed around Prometheus for a less extensive area (southeast of the ring). In addition, in the areas surrounding the Amirani dark lava flows, the mean value of the spectral ratio is higher than the level generally observed over the equatorial plains of Io as reported by *Douté et al.* [2001a]. This implies that Amirani is an important source of SO_2 through degassing or sublimation. This activity is probably linked with the existence of one or more volcanic plumes that erupt from the same vent as the lava flow, are caused by sublimation of an SO_2 snowfield as proposed for Prometheus, or are a combination of both mechanisms. A north-south gradient for the spectral ratio can also be noticed, indicating possible SO_2 gas transport from Amirani to higher latitudes. These trends are compatible with the conclusions of *Douté et al.* [2001a].

3.2.2. Culann. This current analysis of the I25 Culann data uses the high-resolution image of Culann taken by SSI in that orbit [*McEwen et al.*, 2000]. This higher-resolution image allows us to correlate in greater detail the SO_2 ratio map with surface colors than was done previously by *Lopes-Gautier et al.* [2000a]. For comparison, we show the Tohil Patera SO_2 map discussed by *Lopes-Gautier et al.* [2000], which shows an enhancement of SO_2 coinciding with reddish areas. The SSI Tohil image used is from the C21 orbit. Registration between the NIMS and SSI images was done by resampling the SSI image

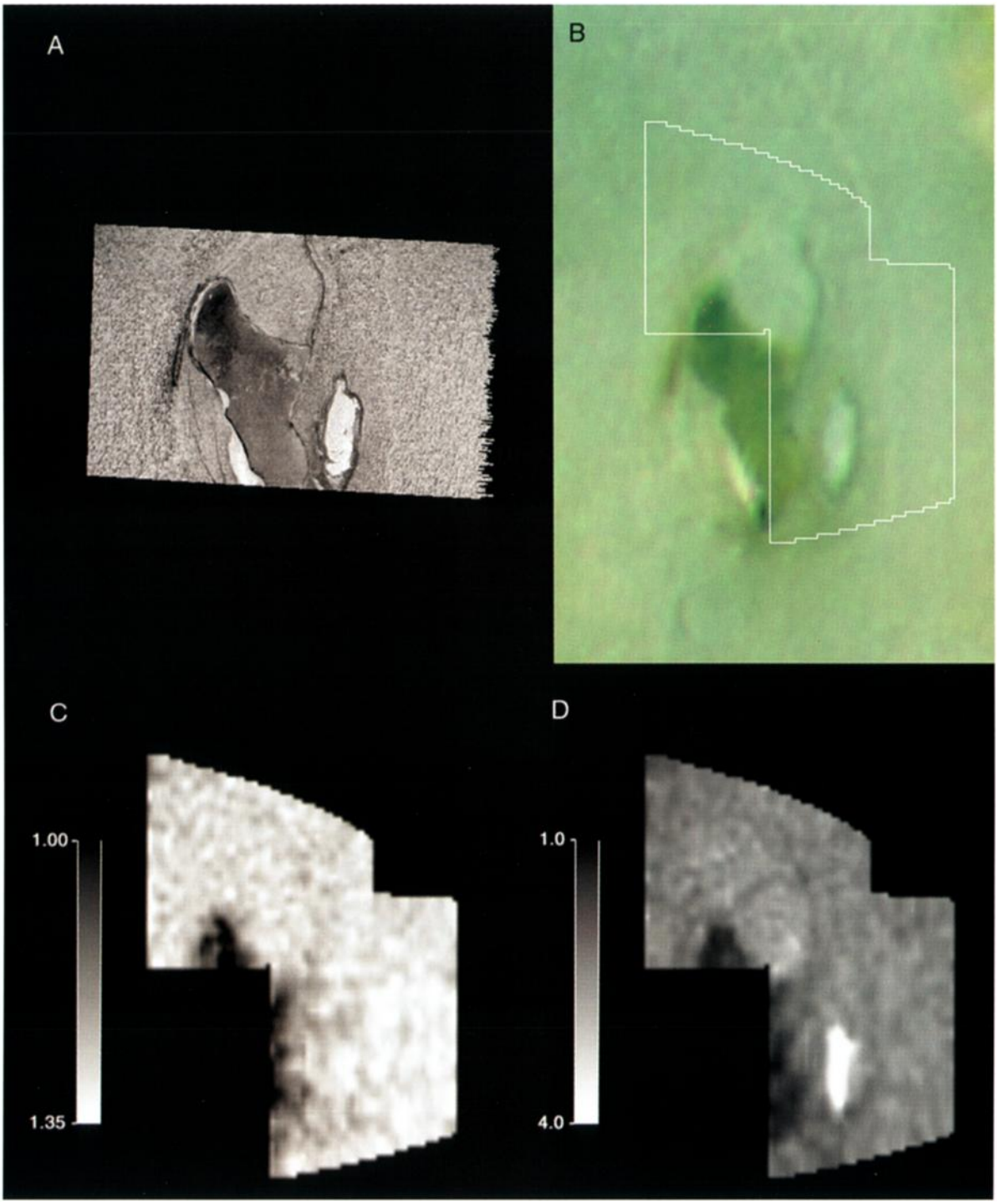

Plate 3. Chaac region as observed by SSI and NIMS during the I27 flyby. (a) SSI high-resolution image from I27. (b) SSI lower-resolution, color image from the C21 orbit, showing dark green materials inside the Chaac caldera. (c) NIMS band ratio map (1.31/1.03 μm) showing the anticorrelation between the depth of the 1-μm absorption and the green deposit in the interior of the caldera. Note that this ratio map is not correlated to albedo, as the ratio shows little variation outside the Chaac caldera. (d) NIMS band ratio map showing the relative abundance of SO_2. The bright white material inside the small caldera just to the east of Chaac (lower right in the camera image) is filled by SO_2 that is purer than at any other location so far observed by NIMS on Io. It may represent a frozen layer of SO_2 ice on the floor of the caldera. The width of the NIMS image is ~100 km.

down to NIMS resolution and comparing albedo profiles to obtain the best match between the two data sets. This was done using the shortest available NIMS wavelength (1.03 μm) and the SSI filter image closest to this wavelength. For Culann we used the SSI filter image at 0.664 μm, and for Tohil we used the SSI image at 0.756 μm, as images in the filter at 0.968 μm, normally used in the coregistering, were not available for either case. The coregistered images are shown in Plate 2. The

NIMS data show enhanced concentrations of SO_2 in the red-colored deposits to the south and north of Culann, as found previously by comparison with the SSI data from C21 [*Lopes-Gautier et al.*, 2000a]. Our new result also shows that the SO_2 ratio is at a local minimum in the regions that have a green coloration in the SSI images. These greenish materials were initially defined by their negative near-infrared spectral slopes in SSI data [*Geissler et al.*, 1999]. Their reflectance reaches a maximum in the SSI green or red filter and then monotonically decreases with wavelength to 1 μm, unlike other Ionian materials that have neutral or positive near-infrared slopes over this wavelength interval. Green materials are also observed in the interior of the Chaac caldera and are discussed further in section 3.2.3.

3.2.3. Chaac. This active caldera has a distinctively green deposit covering its floor [*Geissler et al.*, 1999]. Chaac was detected as a hot spot by NIMS in I25 (25INREGION01). Both NIMS and SSI observed Chaac at high spatial resolution during I27 (Plate 3). The NIMS observation (27INMOSAIC01) only covered part of the caldera. Neither NIMS nor SSI observations covered the hot spot that, according to the NIMS I25 data, is located in the southwestern part of the caldera. *Keszthelyi et al.* [this issue] analyzed the SSI data for Chaac and suggested that low areas of the caldera have been flooded by a bright fluid, similar to what they proposed happened at Tohil Patera. They suggested that nonsilicate fluids are an integral part of Chaac Patera.

The NIMS observation did not cover the southwestern part of the Chaac caldera that is bright in visible wavelengths, discussed by *Keszthelyi et al.* [this issue]. However, the NIMS observation covers a patch of bright material inside a smaller caldera to the east of Chaac (Plate 3), which in visible wavelengths appears similar to the bright material on the edge of Chaac described by Keszthelyi et al. The NIMS data also cover the low-albedo interior of the Chaac caldera and the surrounding plains. The SO_2 band ratio map shows that little SO_2 is present inside the Chaac caldera. This may be due to the current volcanic activity just to the south of the area observed sublimating any SO_2 deposits, or it could be a further indication of the relatively low SO_2 concentration within green-colored areas, as observed in Culann. As with the Amirani nonactive flow described above, recent activity in this area (or nearby) could have caused SO_2 deposits to sublimate.

The band ratio map's most noteworthy result is the extremely high concentration of SO_2 (a surface proportion of 100% if a macroscopic mixing mode is retained, a grain proportion higher than 90% in the case of an intimate mixing) inside the small caldera to the east of Chaac. The high SO_2 concentration in the interior of this small caldera implies a mechanism of deposition in which SO_2 was topographically confined by the caldera walls. This is the purest SO_2 deposit that NIMS has detected on Io and the only one that appears to be topographically confined. *Smythe et al.* [2000] suggested emplacement by liquid flow of SO_2 rising from lower layers. While liquid would normally boil off when exposed to Io's tenuous atmosphere, preliminary estimates by *Smythe et al.* [2000] indicate that given sufficiently large quantities, some of the liquid could freeze to form a layer of sulfur dioxide ice (at least a few millimeters thick) inside the caldera. If this mechanism has taken place, there may be a halo around the caldera where SO_2 that boiled off has recondensed. Neither NIMS nor SSI data show a halo, though it could be transparent in visible wavelengths if the frost is thin (as discussed above and by *Geissler et al.* [this issue]).

The frequency of occurrence for deposits similar to this cannot be estimated from the current Io data set, because the size of the feature, ~100 km^2, is below the spatial resolution of the available regional spectral ratio maps of Io. The observation from which this feature was detected (27INMOSAIC01) has a spatial resolution ranging from 1.7 to 5.3 km/pixel. This feature is present but cannot be detected as a bright SO_2 deposit in maps made from NIMS observations at spatial resolutions of 9–10 km/pixel (27INCAMAXTLI) and 20–30 km/pixel (25INREGION01 and 27INREGION01).

The anticorrelation between green deposits and local SO_2 enhancement observed at Culann is also observed at Chaac (Plate 3). The local SO_2 minima in both areas could be due to proximity to warm, active regions or to differences in origin between the red (possibly mixed pyroclastics from the gas phase) and the green (possibly emplaced lavas) materials. High-resolution images from SSI [*McEwen et al.*, 2000] show that the greenish coloration is restricted to calderas and lava flows, suggesting that they may be formed through alteration or contamination of sulfur deposits by the hot lavas.

It is noticeable that the broad 1-μm absorption identified in NIMS data by *Carlson et al.* [1997] is anticorrelated with the green material inside Chaac (Plate 3) [also *Lopes-Gautier et al.*, 2000b]. This suggests that the areas having a negative near-infrared slope (from red to 1 μm [*Geissler et al.*, 1999]) also have a negative slope from 1 to 1.5 μm and hence do not show the broad absorption centered at around 1 μm. This is not characteristic of pure sulfur or SO_2 compounds, but one possible compositional candidate is sulfur contaminated by iron, such as pyrite, as suggested by *Kargel et al.* [1999]. Other possibilities include sulfur radiolysis products and sulfur contaminated by trace elements [*Carlson et al.*, 2001; *Douté et al.*, 2001b].

4. Thermal Mapping

NIMS data from the flybys allow us to map the thermal structure within hot spots for the first time. This could not be done from any previously acquired data because the sizes of the pixels were so large that they contained a mix of many different types of terrain of varying albedos and temperatures and also several different hot spots. Therefore previous work focused on thermal analysis of a limited set of observations obtained during nighttime in which there was no reflected light component [e.g., *Lopes-Gautier et al.*, 1997; *Davies et al.*, 2000a]. The large sizes of the NIMS pixels (at least 120 km × 120 km) of the distant observations made it impossible to observe the albedo associated with individual hot spots. During the close flybys, the much smaller pixel sizes that fall within the hot spots allowed us to model the albedo and obtain temperatures of hot spots seen under illuminated conditions. The albedo is estimated as a function of the shorter wavelengths in the NIMS range where the radiance from thermal emission is negligible compared with the radiance from reflected sunlight. At wavelengths between 3 and 5 μm the contribution from reflected sunlight is no greater than 20% of the thermal signal, so slight errors in albedo estimates have small effect on the derivation of temperature.

A NIMS pixel showing volcanic activity most likely contains lavas at a range of different temperatures. Techniques for deriving temperatures from NIMS observations, and some of

the associated constraints, were discussed previously [*Lopes-Gautier et al.*, 1997; *Davies et al.*, 1997]. In the presence of sunlight it is not possible to use two-temperature fits to the Planck function in order to derive the "hot component" because the signal at the shorter wavelengths is dominated by reflected sunlight. Therefore, for the daytime observations obtained during the flybys, fitting more than one temperature is not feasible. A single temperature can thus be regarded as a lower estimate of the temperature range present in the pixel. In the case of the Zamama hot spot observed during Galileo's first orbit, a single-temperature fit gave a result that was within 70 K of the cooler component of the two-temperature fit [*Davies et al.*, 1997]. It must be noted that the physical environment of a hot spot is more complex than can be described by a two-component model, although such a model has been shown to give a fairly good fit to the spectra of some terrestrial lavas [*Crisp and Baloga*, 1990; *Flynn and Mouginis-Mark*, 1992].

We present our results in terms of two types of temperatures, the brightness temperature T_B and the color temperature T_C. The brightness temperature is just a convenient representation of the emitted thermal radiation measured by the instrument in a form that is more intuitive than when expressed in radiation units. The brightness temperature can be used to distinguish between measurements of sky, Io's background, and hot spots on the surface, but it provides an accurate temperature measurement only when the pixel is completely filled by this single temperature blackbody. The color temperature (T_C), however, represents the physical temperature of a blackbody that is assumed to model one component of a hot spot. The defining equations are

$$B(\lambda, T_B) = I(\lambda) \quad (1)$$

$$B(\lambda, T_C) = fI(\lambda), \quad (2)$$

where B is the Planck function, λ is the wavelength, I is the corrected radiance, and f is the fractional pixel area, all for a given spatial pixel. Note that T_B is a function of wavelength, but T_C and f are, for a given pixel, constant over the whole spectrum. We assume surface emissivity to be 1. If emissivity is <1, then our brightness temperatures will be underestimates.

For daytime observations the corrected radiance is defined as $I(\lambda) = I_0(\lambda) - AF(\lambda)$, where $I_0(\lambda)$ is the observed radiance, $F(\lambda)$ is incident solar flux at that wavelength and A is an albedo (bidirectional reflectance) estimate derived from the 1–2 μm region. For nighttime observations, $I = I_0$.

Equation (1) is a straightforward calculation, but (2) must be solved as a fit to a set of points. For the latter, we use as cost function the sum of the squares of the differences between computed and observed spectra divided by the estimated errors ("chi-square"). The fit is done using the method of "simulated annealing" described by *Metropolis et al.* [1953], a good description of which is given by *Press et al.* [1986]. This is not a deterministic algorithm but allows stochastic variations within a gradually decreasing range and is particularly well-suited for highly nonlinear problems with many local minima. This was applied to each pixel for which at least four wavelengths were observed in the range 2.5–5 μm (which contains up to eight NIMS wavelengths). In this range, thermal emission dominates reflected sunlight for temperatures greater than ~300 K.

In dayside observations T_B and, in particular, T_C are sensitive to the albedo used to correct the observed radiances, both in amplitude and slope. The albedo is computed from the shorter wavelengths in the NIMS range (1–2 μm) and applied as a correction to the longer wavelengths (beyond 2.4 μm).

Pixels where $T_B < 200$ K are omitted, as otherwise the signal/noise in the thermal component is too low to yield a reliable solution to (2) and also the strong SO_2 absorption at 4.1 μm affects the shape of the spectrum. The strong SO_2 absorption disappears in hot regions (except in the case of Emakong, described in section 4.3). Correct albedo values should yield $I(\lambda) = 0$ for the cold areas of Io. Small residual uncertainties in the NIMS calibration can sometimes yield a spurious $T_B \sim 180$ K for these areas, but these pixels were not used in the analysis.

4.1. Hot Spots in the Prometheus Region

Hot spots and plumes have been detected and monitored by NIMS and SSI from distant observations prior to the Io flybys. Table 2 (updated from *Lopes-Gautier et al.* [1999]) lists the active volcanic regions known on Io from Galileo, Voyager, ground-based, and Hubble Space Telescope (HST) observations. We now know of 97 major active volcanic regions on Io and 27 locations that are possibly active volcanic centers but await confirmation (Table 3). The flyby observations revealed 16 additional hot spots not previously known. These could be sites of new volcanic activity but given that most are faint hot spots, it is more likely that they were not previously detected in lower spatial resolution observations. It is noteworthy that 14 of these new detections came from the NIMS region observations (Table 1 and Plate 4) that together cover an area around Prometheus equivalent to ~5% of Io's surface, at spatial resolutions ~10 times higher than the distant global observations. Prior to the flyby observations, only four hot spots (Prometheus, Camaxtli, Tupan, and Culann) had been resolved in this area.

It is possible to use the distribution of hot spots in this area to estimate the total number of hot spots on Io by inferring the overall global distribution of volcanic centers. *Carr et al.* [1998] mapped active and inactive volcanic centers and concluded that the distribution is uniform at mid and low latitudes, but there may be fewer hot spots at high latitudes. The same conclusion was reached by *Lopes-Gautier et al.* [1999] on the basis of the distribution of known active hot spots. If we assume the global distribution of hot spots to be uniform (including the polar regions), we can expect Io's surface to have around 300 hot spots of brightness similar to those that were detected from the NIMS region observations. However, there are suggestions of a concentration of active and inactive volcanic centers near the sub-Jovian and the anti-Jovian regions [e.g., *Schenck and Hargitai*, 1998; *Radebaugh et al.*, this issue]. Prometheus is located near the anti-Jovian point. The paucity of high-resolution data on the sub-Jovian hemisphere, plus uncertainty in the distribution of hot spots in the polar regions, does not allow us to quantify how much richer in hot spots the Prometheus region is relative to the rest of Io's surface. However, we can use the work of *Radebaugh et al.* [this issue] to make an estimate that the Prometheus region has, at most, twice the concentration of active volcanic centers as other regions on Io. In this case, we can expect a minimum of 150 hot spots on Io. Therefore we now know the locations of at least one third, and possibly up to two thirds, of the expected hot spots on Io.

NIMS observations from the flybys (at resolutions from 1 to 20 km/pixel) show that some individual hot spots, such as Prometheus and Amirani, have more complex thermal struc-

Table 2. Active Volcanic Centers on Io: Detections of Plumes and Hot Spots by Galileo, Voyager, HST, and Ground-Based Observations[a]

Volcanic Center	Location of Candidate Surface Feature	SSI Hot Spot	Location Galileo NIMS	Voyager IRIS Hot Spot?	Ground-Observed or NICMOS (N) Hot Spot?	Plume? (V, G, C)	Surface Change?	Notes
Ruwa Patera[b]	1°N, 3°W	1°N, 2°W			9812A?[b]	no	no	faint bright spot in SSI G8 eclipse image, confirmed in E14
Nusku Patera	63°S, 7°W			yes?		no	no	
Mbali Patera	32°S, 8°W			yes		no	no	red deposits
Unnamed[b]		10°S, 14°W			9606C? 9906A?[b]	no	no	detected by SSI in C21, bright spot in SSI G8 eclipse image
Karei Patera?	2°N, 16°W	yes?			9608A? 9812A?[b]	no	no	
Ukko Patera	32°N, 20°W				9508A?	no	yes	
Uta Patera	35°S, 25°W			yes?	9606C?, N15?, D?	no	no	very low albedo
Kanehekili, north and south	18°S, 37°W	14.5°S, 33.4°W 17.2°S, 35.5°W	12° ± 10°S, 34° ± 4°W		yes, N5	G	yes	
Unnamed (north polar)	70 ± 15°N, 35 ± 15°W				9610A	no	yes	north polar changes seen by SSI, unclear if location consistent with hot spot detected from the ground
Janus Patera	3°S, 40°W	4°S, 39°W	4 ± 5°S, 42 ± 5°W		9606A?, N2, D	no	no	
Masubi	44°S, 55°W		53 ± 12°S, 52 ± 12°W		9808A?[b]	V	yes	new plume deposits and hot spot detected by SSI in E11; hot spot detected by J. Spencer on Aug. 29, 1998 (faded by Aug. 31, 1998)
Unnamed					0002A			detected by J. Spencer and R. Howell at 60° ± 15°N, 60° ± 15°W
Shamshu	10°S, 63°W		10 ± 4°S, 67 ± 4°W			no	no	
Tawhaki[b]	3°N, 76°W	3.8°N, 76.1°W	12 ± 8°N, 73 ± 8°W		yes? (9908A)	no	no	detected in E11 by SSI; possible site of outburst detected on Aug. 2, 1999, by R. Howell; hot spot detected by NIMS in C21
Unnamed (Poliahu?)[b]			35 ± 8°S, 77 ± 8°W		yes?	no	no	detected by NIMS in E11, possibly same as *Goguen et al.*'s [1988] hot spot (Table 3)
Zal Patera	41°N, 76°W	36.3°N, 76.1°W	43 ± 7°N, 78 ± 10°W			no	yes	bright red deposits
Hi'iaka Patera	2°S, 79°W		1 ± 4°S, 76 ± 4°W		yes	no	yes	
Gish Bar Patera	17°N, 90°W	16.3°N, 91°W	16 ± 4°N, 89 ± 5°W			no	no	
Unnamed[b]		46°N, 92°W				no	no	detected by SSI in E15
Sigurd Patera	5°S, 97°W		5 ± 4°S, 100 ± 4°W			no	no	
Itzamna	16°S, 98°W		15 ± 3°S, 97 ± 3°W			no	no	
Arusha Patera?	38°S, 101°W				9503A			outburst detected by J. Spencer
Monan Patera	19°N, 106°W		19 ± 3°N, 106 ± 4°W			no	no	
Altjirra Patera	35°S, 109°W		33 ± 4°S, 108 ± 4°W	yes, same as Malik?		no	yes	bright red deposits
Amirani	25°N, 116°W	23.2°N, 116.3°W	27 ± 4°N, 112 ± 4°W	yes		V, G	yes	bright red deposits
Dusurra[b]	37°N, 118.5°W		39 ± 7°N, 125 ± 7°W			no	no	NIMS C21 hot spot, low albedo
Emakong[c]	3°N, 119°W		3 ± 1°S, 119 ± 1°W			no	no	detected by NIMS in I27
I27E (NW of Amirani)[c]	31.4°N, 116.7°W		31 ± 0.5°N, 117 ± 0.5°W			no	no	detected by NIMS in I27
Maui (plume site)	20°N, 122°W		19 ± 3°N, 122 ± 3°W	yes, same as Amirani?		V	yes?	Voyager plume obscures surface
Tvashtar Catena[c]	63°N, 122°W				yes (1999) C	yes		detected by NIMS and SSI in I25, I27, and G29; new Pele-type plume deposit detected in G29

Table 2. (continued)

Volcanic Center	Location of Candidate Surface Feature	SSI Hot Spot	Location Galileo NIMS	Voyager IRIS Hot Spot?	Ground-Observed or NICMOS (N) Hot Spot?	Plume? (V, G, C)	Surface Change?	Notes
I27C (Maui Patera?)[c]	16.2°N, 123.8°W		16.5 ± 1°N, 124 ± 1°W					detected by NIMS in I27
Malik Patera	35°S, 128°W		35 ± 3°S, 127 ± 3°W	yes		no	no	bright red deposits
"Emakong flow" (Seth?)[c]			5 ± 1°S, 132 ± 1°W					detected by NIMS in I25 and I27
I27B			20±°N, 131 ± 1°W					detected by NIMS in I27
Camaxtli (9805A)[b]	16°N, 137°W	16°N, 136°W	15° ± 3°N, 137° ± 3°W			no	no	detected in E15 by NIMS, SSI
"Main" (9805A)[c]			14.5 ± 1°N, 136 ± 1°W					detected by NIMS in I24, I27
"c"[c]			9.5 ± 1°N, 132 ± 1°W					detected by NIMS in I25, I27
"East"[c]			12 ± 1°N, 134 ± 1°W					detected by NIMS in I24, I27
"West"[c]			15 ± 1°N, 139 ± 1°W					detected by NIMS in I24, I27
Unnamed (north polar)	65°N, 141°W	65.2°N, 132°W				no	no	
Tupan Patera	18°S, 141°W		17 ± 3°S, 141 ± 3°W			no	no	bright red deposits
I25A (Cuchi Patera?)[c]	0.6°N, 145.8°W		2 ± 1°S, 144 ± 1°W					detected by NIMS in I25
I24A (near Surya)[c]			22 ± 1°N, 146 ± 1°W			no	no	detected by NIMS in I24, I27
Arinna Fluctus (9606W)	32°N, 147°W		36 ± 6°N, 147 ± 6°W			no	yes	bright red deposits
I24B[c]			14° ± 1°N, 150 ± 1°W			no		detected by NIMS in I24 and I27
I27A (Surya)[c]	22°N, 151°W		22 ± 1°N, 152 ± 1°W			no	yes	detected by NIMS in I27, surface change detected by SSI
Shamash Patera	34°S, 153°W		33 ± 6°S, 157 ± 6°W	yes, same as Malik?		no	no	
Prometheus	2°S, 154°W		1 ± 3°S, 155 ± 3°W			V, G	yes	bright red deposits, plume moved between Voyager and Galileo
"West hot spot"[c]								
"Center hot spot"[c]								
"East hot spot"[c]								
Chaac	11°N, 158°W		10°N, 157°W					bright green deposits, detected by NIMS in I25 and I27
Culann Patera	19°S, 160°W		18 ± 3°S, 163 ± 3°W			G?	yes	bright red deposits
I27D[c]			0, 164°W					
Zamama	18°N, 173°W	18.9°N, 172°W	21 ± 3°N, 173 ± 3°W			G	yes	bright red deposits
Volund	23°N, 176°W		25 ± 3°N, 174 ± 3°W	yes		V	yes	
Aidne Patera	1°S, 177°W		2 ± 3°S, 178 ± 3°W			no	yes	
Haokah (9803B)[b]	20.9°S, 186.7°W		19 ± 3°S, 185 ± 3°W			no	no	bright green deposit in SSI images, hot spot detected by NIMS in E11, E14
Fo Patera	40°N, 192°W	40.1°N, 200.8°W	39 ± 3°N, 191 ± 3°W			no	yes	
Sethlaus Patera	52°S, 194°W		50 ± 3°S, 195 ± 3°W			no	no	red deposits
Rata Patera	35°S, 199°W		35 ± 3°S, 199 ± 3°W			no	no	red deposits
Lei-Kung Fluctus	36°N, 203°W		37 ± 3°N, 206 ± 3°W			no	no	bright red deposits
Gabija (9803E)[b]	52°S, 203°W		52 ± 3°S, 204 ± 3°W			no	no	hot spot detected by NIMS in E14
Isum Patera, north	29°N, 209°W	32.9°N, 204.7°W	31 ± 3°N, 207 ± 3°W	yes	9510A?	no	no	bright red deposits
and south	30.3°N, 206.8°W							

Marduk	27°S, 209°W	27.1°S, 209.1°W	26 ± 3°S, 212 ± 3°W	yes		V, G	yes	bright red deposits
Unnamed (Lei-Kung source?)[c]	65°N, 215°W							detected by PPR in I25
Kurdalagon Patera	50°S, 218°W		47 ± 3°S, 219 ± 3°W			no	no	red deposits
Ot (9611A)	2°S, 218°W		47 ± 3°S, 218 ± 3°W			no	no	
Mulungu Patera	17°N, 218°W	17.6°N, 216.8°W	17 ± 3°N, 219 ± 3°W		9510A?	no	no	
Susanoo (9803D)[b]	22°N, 220°W		21 ± 3°N, 222 ± 3°W		9510A?	no	no	hot spot detected by NIMS in E14
Wayland (9803C)[b]	32°S, 226°W		30 ± 3°S, 224 ± 3°W			no	no	hot spot detected by NIMS in E14
Reiden Patera	13°S, 236°W	12.5°S, 234.9°W				no	no	
Girru (9803A)[b]	22°N, 240°W		22 ± 3°N, 238 ± 3°W			no	no	hot spot detected by NIMS in E14, E15
Pillan Patera, and N&S	12°S, 244°W	9.9°S, 242.3°W	13 ± 3°S, 244 ± 3°W			G	yes	major change in 1997; plume also detected by HST
		9.5°S, 242.7°W						
		11.5°S, 242.2°W						
Pyerun Patera	55°S, 252°W			yes, same as Mithra?		no	no	
Pele	18°S, 256°W	18°S, 256°W	20 ± 3°S, 255 ± 3°W	yes		V, G	yes	large, bright red deposits
Shakura Patera	24°N, 267°W			yes, same as Daedalus?		no	no	very low albedo; detected as hot spot by PPR in I27 [*Spencer et al.*, 2000][c]
Mithra Patera	59°S, 267°W			yes, same as Pyerun?		no	no	red deposits
Svarog Patera	48°S, 268°W	53.9°S, 270°W	42° ± 5°S, 269° ± 5°W	yes		no	no	
Babbar Patera	39°S, 273°W		37 ± 4°S, 283 ± 8°W	yes		no	no	
Daedalus Patera	19°N, 275°W		18 ± 3°N, 273 ± 3°W	yes		no	yes	red deposits; detected as a hot spot by PPR in I27 [*Spencer et al.*, 2000][c]
Viracocha Patera	62°S, 282°W			yes		no	no	
Ulgen Patera[b]	40°S, 288°W		41 ± 9°S, 291 ± 9°W	yes	N6?, D?	no	no	very low albedo, detected by NIMS in C22, possibly "merged"with Babbar in prior observations
Sengen Patera?	32°S, 304°W				9506J?, N6?, D?	no	yes	
Amaterasu Patera	38°N, 307°W		40 ± 4°N, 309 ± 4°W	yes	maybe	no	yes	especially low albedo (usually)
Loki Patera	13°N, 309°W	10.8°N, 310.5°W	9 ± 7°N, 309 ± 7°W	yes	ground, N1	V	yes	
Dazhbog Patera?[b]	56°N, 303°W				N13	no	yes	NICMOS (66.4 ± 8°N, 310.6 ± 14°W)
Aten Patera	48°S, 311°W			yes	N9, D?	no	yes	Pele-type plume deposits, reddish
Mazda Catena	8°S, 314°W			yes	N7?, D?	no	no	red deposits
Kinich Ahau (NICMOS 11)[b]	49°N, 312°W				N11	no	no	NICMOS (50.3 ± 5°N, 318.8 ± 8°W)
Nemea	80°S, 320°W			yes		no	no	
Unnamed[b]	40.5°S, 326.3°W		36 ± 9°S, 324 ± 9°W			no?	no	detected by NIMS in C22
Ra Patera	8°S, 325°W					G	yes	major brightening observed by HST in 1994 [*Spencer*, 1987]
Fuchi Patera	29 N, 328 W	29 N, 327 W[b]			9606G?, N4, D	no	no	Red deposits, hot spot detected by SSI in E14
Acala Fluctus	11 N, 336 W	10.7 N, 333.2 W		yes	N3, D	G	yes	Detected by PPR in 127 [*Spencer et al.*, 2000][c]
Surt	46°N, 338°W				9606E?, N12	no	yes	Pele-type plume deposits, reddish
Creidne Patera	53°S, 344°W			yes	N8?	no	yes	
Tiermes Patera?	23°N, 351°W				9507A	no	no	
Euboea Fluctus?	45°S, 352°W				9606F?, N8?, D?	no	yes	Pele-type plume deposits, bright red
Fjorgynn Fluctus	12°N, 358°W				9606D?, N10, D	no	yes	
Unnamed[b]					D	no	no	detected by C. Dumas on June 3, 1998 at 6 ± 3°S, 358 ± 3°W; possibly same as SSI G8 faint spot at 2°S, 352°W

[a]N, NICMOS hot spots detected by *Goguen et al.* [1988]. D, hot spots detected by C. Dumas et al. (personal communication, 1997, 1998). Other ground-based hot spots detected by *Spencer et al.* [1997a]. V, G, C, Voyager, Galileo, or Cassini detection.

[b]Major changes since C10 data published by *Lopes-Gautier et al.* [1999].

[c]I24, 25, and 27 detections.

Table 3. Identifications of Possibly Active Volcanic Centers[a]

Volcanic Center	Location of Candidate Surface Feature	SSI Hot Spot?	Ground-Observed Hot Spot?	Plume?	Surface Change?	Notes
Unnamed		15.3°N, 4.7°W	9606D?	no	no	faint bright spot in SSI G8 eclipse image
Unnamed		2°S, 13°W		no	no	faint bright spot in SSI G8 eclipse image
Unnamed		11.5°N, 13.3°W		no	no	
Unnamed		5.2°N, 24.1°W		no	no	faint bright spot in SSI G8 eclipse image
Unnamed		6°S, 19°W		no	no	faint bright spot in SSI G8 eclipse image
Unnamed		1°N, 21°W		no	no	faint bright spot in SSI G8 eclipse image
Unnamed		1°S, 23°W		no	no	faint bright spot in SSI G8 eclipse image
Unnamed		9°S, 27°W		no	no	faint bright spot in SSI G8 eclipse image
Unnamed		13.1°S, 22.8°W	9606C?	no	no	faint bright spot in SSI G8 eclipse image
Unnamed		16.5°S, 27.9°W	9606C?	no	no	faint bright spot in SSI G8 eclipse image
Lei-zi[b]	10°N, 45°W	no		no	yes	
Unnamed (NICMOS)		no	NICMOS 14	no	no	faint NICMOS spot at 54.4° ± 5°N, 60.1°W (error in latitude up to −18°)
"Poliahu"	19.4°S, 81.8°W	no	yes	no	no	reported at 22° ± 5°S, 79° ± 5°W by *Goguen et al.* [1988]
Ekhi[b]	26°S, 88°W	no		no	no	
Shango[b]		32°N, 100°W		no	no	faint bright spot in SSI—eclipse image
Catha Patera	53°S, 100°W	no		no	yes	
Unnamed	42°N, 134°W	no		no	yes	reddish materials
Unnamed	31°N, 146°W	no		no	yes	large region of red deposits, coordinates are of center
Unnamed	22°S, 168°W	22°S, 168°W		no	no	SSI faint spot in E11
Namarrkun[b]	11°N, 175°W	no		no	no	
Donar[b]	24°N, 185.5°W	no		no	no	
Unnamed		28.5°N, 189.4°W		no	no	
Unnamed	38°S, 291°W	no		no	no	low albedo and bright red materials
Huo Shen Patera	15°S, 330°W	no		no	no	HST changes [*Spencer et al.*, 1997] not confirmed by SSI
Unnamed		17.1°N, 332.9°W		no	no	
Unnamed		2°S, 352°W		no	no	faint bright spot in SSI G8 eclipse image; possibly same as hot spot detected by C. Dumas on June 3, 1999
Unnamed		4.8°N, 356.1°W		no	no	

[a]Updated from *Lopes-Gautier et al.* [1999].
[b]Major changes from *Lopes-Gautier et al.* [1999].

tures than could be detected at global scales. Thermal maps from the flyby observations, discussed below, show different styles of eruption for different hot spots. Analysis of the three region observations also shows that significant variations in level or activity occur at short timescales. Table 4 is a comparison of hot spots in all three region observations and it states whether each hot spot was observed and whether or not it was detected. Color temperatures (T_C) were obtained by the method explained above for all the cases when there were sufficient data points (less than four wavelengths) and the error returned by the Metropolis fitting algorithm (see above) was <30%. In a few cases, an approximate color temperature is given based on fewer data points (three wavelengths), and errors can be as high as 50%. We also report the power at 4.7 μm. This wavelength was chosen for two reasons. First, it is the longest wavelength available in the flyby data set and has the lowest signal from the solar flux in daytime observations. Second, to facilitate comparisons with ground-based observations [e.g., *Veeder et al.*, 1994]. The power (emitted into a hemisphere) was derived using

$$P(4.7\ \mu\text{m}) = (RA)/\cos(E), \quad (3)$$

where $P(4.7\ \mu\text{m})$ is power at 4.7 μm (in units of W μm^{-1}); R is observed radiance (W m^{-2} sr^{-1} μm^{-1}), corrected for background radiation; A is emitting area (m^2) equal to S*FOV, where S is the slant distance and FOV is the field of view of the NIMS pixel (in the case of a NIMS data cube) or the field of view of the NIMS detector (in the case of a NIMS data tube); and E is the emission angle; cos (E) is applied to correct to vertical perspective.

The background is the median of the radiances from a 20 × 20 pixel area, excluding the hot spot pixels themselves. We assume that the albedo at 4.7 μm is constant between the background and the hot spots. If the hot spots are darker at 4.7 μm than they are in the visible, then the power reported will be an underestimate. However, the differences will be constant between observations for a given hot spot.

The calculation was done using one of two methods, depending on whether the hot spot was considered an extended source (over several NIMS pixels) or a subpixel source, one using resampled data (NIMS "cubes") and the other using original unresampled data (NIMS "tubes"). For an extended source, NIMS data cubes were used and (RA) was summed over all pixels in the vicinity of the hot spot having R over a threshold of twice the background value. In the case of Prometheus, because of the large extent of the hot area (Plate 5), three values were obtained: west, middle, and east.

In the case of a subpixel source the NIMS projection algorithm used to make data cubes can introduce errors in the integrated radiance because of the nonuniformity of the NIMS

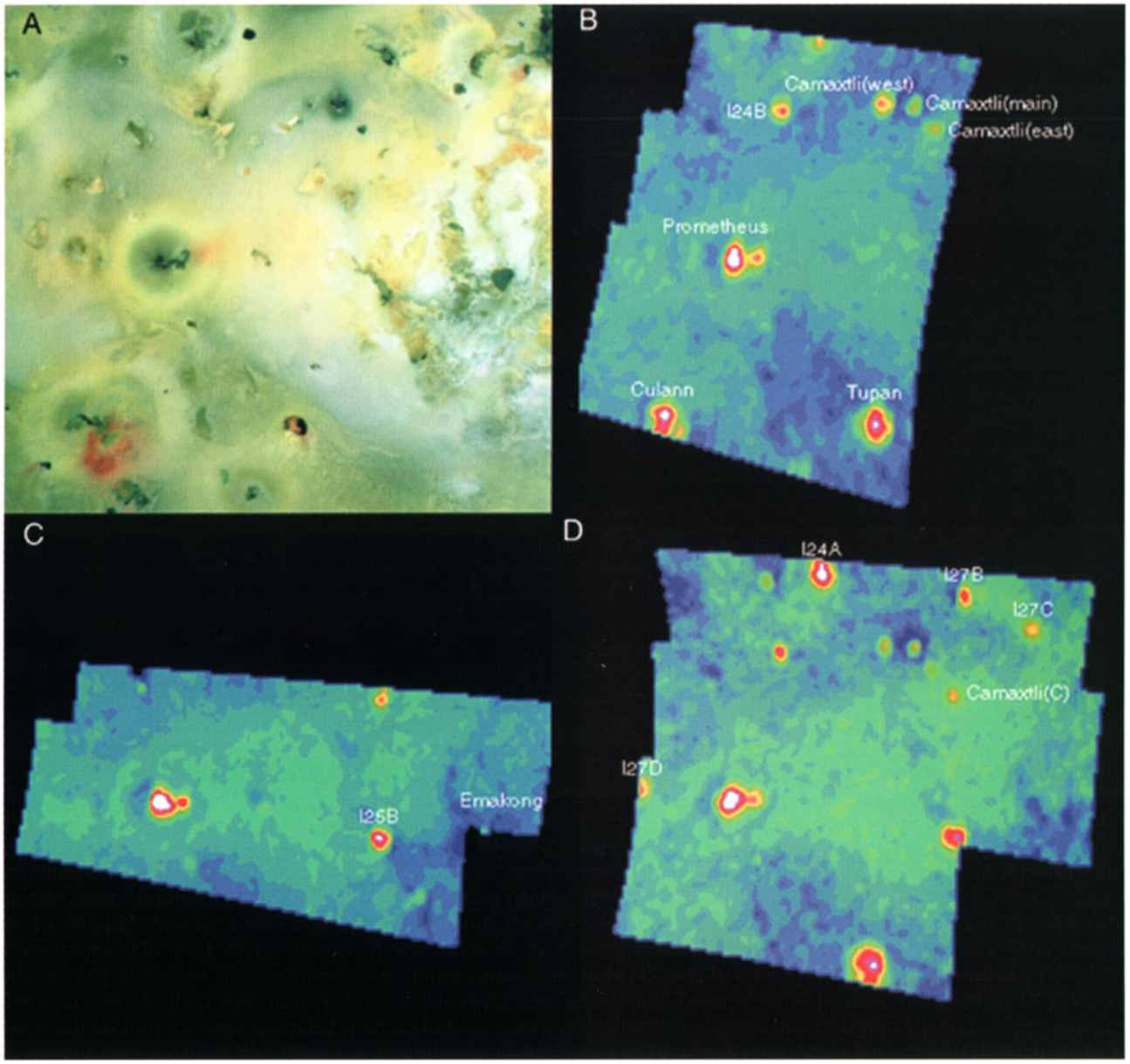

Plate 4. Western part of Bosphorus Regio and the Prometheus region as observed by NIMS during (b) I24, (c) I25, and (d) I27. These region observations had spatial resolutions of approximately 25 km/NIMS pixel. (a) A SSI image of the region covered by NIMS. The NIMS observations are shown here as 4.8-μm maps, and the hot spots are shown as yellow to red to white areas. See Table 1 for observation details and Table 4 for hot spot temperature and power.

detector response function [*Carlson et al.*, 1992]. Therefore, in these cases, original NIMS data tubes were used (an array of unresampled original NIMS radiances). Adjacent mirror steps in the tubes were co-added to take into account the NIMS response function, and the background value was adjusted accordingly. For each hot spot a histogram was formed of all the tube pixels showing a contribution from the hot spot (usually 10–20 pixels because of the slow slew rates during these observations). The peak of the histogram was taken as the radiance (R) of the hot spot and used in the above equation. The data tube method was also used to double-check the power calculations for some extended sources. In these cases, the power calculated using data tubes was in substantial agreement with that obtained from cubes.

The power at 4.7 μm was computed in order to search for variations in power output between hot spots. As can be seen from Table 4, the power at 4.7 μm for Tupan, Culann, and Prometheus is significantly larger ($>45 \times 10^8$ W m^{-2}) than the values for most of the hot spots that were detected for the first time from the high-resolution data (most yielded power $<10 \times 10^8$ W m^{-2}).

Significant variations in power at 4.7 μm between orbits were observed for hot spots Camaxtli "c" (~40% decrease from I25 to I27), Camaxtli "west" (~75% decrease from I24 to I27), and Tupan (~30% increase from I24 to I27). We can qualitatively suggest that changes in power output may have happened at hot spots I25A, Chaac, and I27D, as these hot spots were observed at similar spatial resolution in more than

one orbit but not detected in all orbits. We give upper limits for the power for these hot spots based on the detectable upper limit of radiance in the NIMS tubes pixels.

4.2. Lava Flow Activity: Prometheus and Amirani

Prometheus and Amirani are two persistent hot spots on Io that were observed to be active by Voyager and repeatedly by Galileo [*Lopes-Gautier et al.*, 1999]. One difference in their history is that the Prometheus flow has increased in length by some 80 km between the Voyager flybys in 1979 and the first Galileo observations in 1996 [*McEwen et al.*, 1998a]. The Amirani-Maui flow field is ~300 km in length and includes the longest active lava flows known in the solar system [*Keszthelyi et al.*, this issue]. *McEwen et al.* [2000] interpreted the Prometheus flow as a long-lived, tube-fed, compound pahoehoe flow field. *Keszthelyi et al.* [this issue] proposed that the Amirani-Maui region is a complex, compound flow field. Here we use thermal data from NIMS to map these two flows and obtain clues to their emplacement styles.

4.2.1. Prometheus. One of the most interesting results from the high-resolution observations was the movement of the Prometheus plume. Observations by SSI during Galileo's first orbit in 1996 showed that the Prometheus plume site had moved ~80 km west since 1979 [*McEwen et al.*, 1998a], but the size and appearance of the displaced plume had not changed. Observations by SSI in I24 showed a caldera just to the north of the Voyager plume site [*McEwen et al.*, 2000] and a long lava flow between the Voyager and Galileo plume sites. The NIMS observation in I24 of the same region [*Lopes-Gautier et al.*, 2000a] showed two main hot spots, one in the east and another in the western part of the flow, though thermal emission can be detected along the whole flow. The eastern hot spot is near the location of the 1979 plume, while the western hot spot is at the location of the current plume. SSI and NIMS data analysis [*McEwen et al.*, 2000; *Lopes-Gautier et al.*, 2000a] showed that the likely vent area for the lava flow is located just south of the Prometheus caldera, in the region where NIMS detects the highest temperatures. The conclusion based on the NIMS and SSI I24 data was that the vent associated with the eastern hot spot did not move. Instead, the plume moved to the western hot spot, even though the eastern hot spot remained active. *Kieffer et al.* [2000] modeled the plume's movement in terms of the interaction between hot lava and the underlying SO_2 snowfield.

Prometheus was observed by NIMS again in I27 (27INPROMTH01) at spatial resolution under 7.5 km pixel^{-1}. A temperature map was obtained from the NIMS data, and this was matched to the SSI observation of the same area (Plate 5). The temperature map shows that the highest temperature that could be reliably determined (based on four wavelengths) is 910 ± 40 K. This is at the eastern end of the flow, near the proposed vent area. Neighboring pixels in the same region may be hotter but have too many saturated wavelengths for a reliable temperature determination to be made. A temperature profile along the flow (Plate 5) shows lower temperatures away from the proposed vent area. Temperatures along the middle of the flow are fairly constant, ranging from 240 K to 460 K. Temperatures rise again at the western end of the flow up to 560 ± 70 K near the site of the present plume. A profile from I24 data (Plate 5) shows the same general pattern and temperatures within the error bars of the I27 values, indicating that at least in the scale of months, the lava flow activity remained steady.

The temperature profile of the Prometheus flow is consistent with that of an insulated lava flow field. Hot material is erupting from a vent in the eastern end of the flow and may be moving through lava tubes, keeping the most of the surface at fairly constant, lower temperatures than at the vent area. At the western part of the flow, close to where the present plume is erupting, the increased temperatures are consistent with lava being exposed and spreading out as it emerges from tubes. This is not a unique interpretation, but it is consistent with the interpretation from SSI images, including those from I27 [*Keszthelyi et al.*, this issue]. SSI analysis of flow images suggests that other than a small active breakout midway down the flow field, no hot lava is exposed until it reaches the western end of the flow field, where it breaks out. In terms of composition, our results (temperatures up to 910 ± 40 K) only provide a lower limit for the eruption temperature, which is likely to be several hundred degrees hotter. The lower limit that we obtained is consistent with a wide range of liquidus temperatures, including those in the ultramafic and basaltic ranges.

Comparison of the results above with those from the NIMS regional observation (27INREGION01) discussed in section 4.1 illustrate well how higher spatial resolution observations are better capable of detecting higher temperatures. Typically, the highest temperatures in a flow field are found in very small areas relative to the total size of the flow field. NIMS data from the regional observation (at spatial resolution of ~25 km pixel^{-1}) could not resolve the highest temperatures (910 ± 40 K) measured from the higher resolution observation (at 7.5 km pixel^{-1}). The regional observation was taken ~1 hour after the high-resolution Prometheus observation and showed top temperatures (allowing for errors) being under 735 K. Prometheus showed little change in temperature between high-resolution observations taken months apart in I24 and I27 (Plate 5), and its activity appears to be at a steady level. The change in peak temperature measured between the high- and low-resolution observations is therefore caused by change in resolution rather than changes in lava temperatures.

4.2.2. Amirani. The Amirani-Maui region is characterized by a long lava flow that runs north-south and a second flow that runs from the main flow west towards Maui (Plate 6). Voyager 1 data showed Amirani and Maui together to be a prominent thermal anomaly [*Pearl and Sinton*, 1982]. Both NIMS and SSI have detected thermal emission from Amirani during the main Galileo mission, and NIMS detected a hot spot near the location of Maui [*McEwen et al.*, 1998a; *Lopes-Gautier et al.*, 1997, 1999]. SSI data from the main Galileo mission showed surface changes in the dark flows between Voyager and Galileo observations [*McEwen et al.*, 1998a].

During I24 and I27, thermal emission was detected by NIMS along the north-south flow and from a caldera to the southwest of the flow that may be the source of the lava. NIMS I27 data showed thermal emission from a small caldera to the northwest of the flows (I27E, Table 2) that appears to be unrelated to Amirani and had not previously been detected as a hot spot. No thermal emission was detected from the flow that runs from the main Amirani flow to the west toward Maui, suggesting that activity has halted in that region. This flow appears to be fed from the same vent as the main Amirani flow. *Keszthelyi et al.* [this issue] suggests that Maui Patera (Plate 6) is unrelated to the flows. The NIMS hot spot Maui (Table 2) reported by *Lopes-Gautier et al.* [1997, 1999] may be located at Maui Patera, however; the spatial resolution of the distant NIMS observations does not allow us to locate the source of the thermal

Table 4. Hot Spots Detected in NIMS Region Observations During I24, I25, and I27

Name	Location	24INREGION01	25INREGION01	27INREGION01
Emakong	3° ± 1°S, 119° ± 1°W	not observed	detected $T_C \sim 300$ K $P(4.7\ \mu m) = (0.2\mu 0.1) \times 10^8$ W μm^{-1}	detected $T_C \sim 300$ K $P(4.7\ \mu m) = (0.4\mu 0.2) \times 10^8$ W μm^{-1}
I27C	16.5° ± 1°N, 124° ± 1°W	not observed	not observed	detected $P(4.7\ \mu m) = (2.3 \pm 0.2) \times 10^8$ W μm^{-1}
I25B "Emakong flow" (Seth?)	5 ± 1°S, 132° ± 1°W	not observed	detected $T_C = 511 \pm 24$ K $P(4.7\ \mu m) = (24.1 \pm 2.4) \times 10^8$ W μm^{-1}	detected $T_C = 514 \pm 20$ K $P(4.7\ \mu m) = (28.9 \pm 3.0) \times 10^8$ W μm^{-1}
I27B	20° ± 1°N, 131° ± 1°W	not observed	not observed	detected $T_C = 531 \pm 33$ K $P(4.7\ \mu m) = (9.8 \pm 1.0) \times 10^8$ W μm^{-1}
Camaxtli "main"	14.5° ± 1°N, 135° ± 1°W	detected $P(4.7\ \mu m) = (2.3 \pm 0.2) \times 10^8$ W μm^{-1}	not observed	detected $P(4.7\ \mu m) = (1.9 \pm 0.2) \times 10^8$ W μm^{-1}
Camaxtli "c"	9.5° ± 1°N, 132° ± 1°W	not observed	detected $T_C = 420 \pm 31$K $P(4.7\ \mu m) - (4.9 \pm 0.5) \times 10^8$ W μm^{-1}	detected $T_C = 380 \pm 114$ K $P(4.7\ \mu m) = (2.8 \pm 0.3) \times 10^8$ W μm^{-1}
Camaxtli "east"	12° ± 1°N, 134° ± 1°W	detected $T_C = 467 \pm 115$ K $P(4.7\ \mu m) = (2.3 \pm 0.2) \times 10^8$ W μm^{-1}	not observed	detected $P(4.7\ \mu m) = (2.0 \pm 0.2) \times 10^8$ W μm^{-1}
Camaxtli "west"	15° ± 1°N, 139° ± 1°W	detected $T_C = 415 \pm 24$K $P(4.7\ \mu m) = (1.5 \pm 0.2) \times 10^8$ W μm^{-1}	not observed	detected $T_C \sim 500$ K $P(4.7\ \mu m) = (0.36 \pm 0.13) \times 10^8$ W μm^{-1}
Tupan	18° ± 1°S, 141° ± 1°W	detected $T_C = 548 \pm 80$ K $P(4.7\ \mu m) = (45.3 \pm 4.5) \times 10^8$ W μm^{-1}	not observed	detected $T_C = 600 \pm 61$ K $P(4.7\ \mu m) = (64 \pm 6.4) \times 10^8$ W μm^{-1}
I25A	2° ± 1°S, 144° ± 1°W	not detected $P(4.7\ \mu m) < 0.3 \times 10^8$ W μm^{-1}	detected $P(4.7\ \mu m) = (0.5 \pm 0.4) \times 10^8$ W μm^{-1}	not detected $P(4.7\ \mu m) < 0.3 \times 10^8$ W μm^{-1}
I24A (near Surya)	22° ± 1°N, 146° ± 1°W	detected (on edge of observation)	not observed	detected $T_C = 378 \pm 23$ K $P(4.7\ \mu m) = (53.0 \pm 5.0) \times 10^8$ W μm^{-1}
I24B	14° ± 1°N, 150° ± 1°W	detected $T_C = 526 \pm 26$ K $P(4.7\ \mu m) = (7.7 \pm 0.8) \times 10^8$ W μm^{-1}	not observed	detected $T_C = 539 \pm 32$ K $P(4.7\ \mu m) = (9.6 \pm 1.0) \times 10^8$ W μm^{-1}
I27A (Surya)	22° ± 1°N, 152° ± 1°W	not observed	not observed	detected $T_C \sim 500$ K $\times 10^8$ W $\mu m^{-1} = (0.9 \pm 0.2) \times 10^8$ W μm^{-1}
Prometheus	2°S, 154°W	detected $T_{west} = 456 \pm 24$ K $T_{min} = 473 \pm 27$ K $T_{east} = 596 \pm 42$ K $P(4.7\ \mu m) = (87.0 \pm 9) \times 10^8$ W μm^{-1}	detected $T_{west} = 473 \pm 3$ K $T_{mid} = 554 \pm 25$ K $T_{east} = 684 \pm 81$ K $P(4.7\ \mu m) = (101.6 \pm 10) \times 10^8$ W μm^{-1}	detected $T_{west} = 472 \pm 1$ K $T_{mid} = 532 \pm 18$ K $T_{east} = 652 \pm 83$ K $P(4.7\ \mu m) - (98.4 \pm 10) \times 10^8$ W μm^{-1}
Chaac	11°N, 158°W	not detected $P(4.7\ \mu m) < 0.3 \times 10^8$ W μm^{-1}	detected $P(4.7\ \mu m) = (0.18 \pm 0.07) \times 10^8$ W μm^{-1}	detected only in higher resolution observation (27INCAMAXTLI) at 9–10 km/NIMS pixel
Culann	19°S, 160°W	detected $T_C = 480 \pm 27$ K $P(4.7\ \mu m) = (54.0 \pm 5.0 \times 10^8$ W μm^{-1}	not observed	not observed
I27D	0, 164°W	not detected $P(4.7\ \mu m) < 0.3 \times 10^8$ W μm^{-1}	not detected $P(4.7\ \mu m) < 0.2 \times 10^8$ W μm^{-1}	detected $P(4.7\ \mu m) = (0.65 \pm 0.25) \times 10^8$ W μm^{-1}

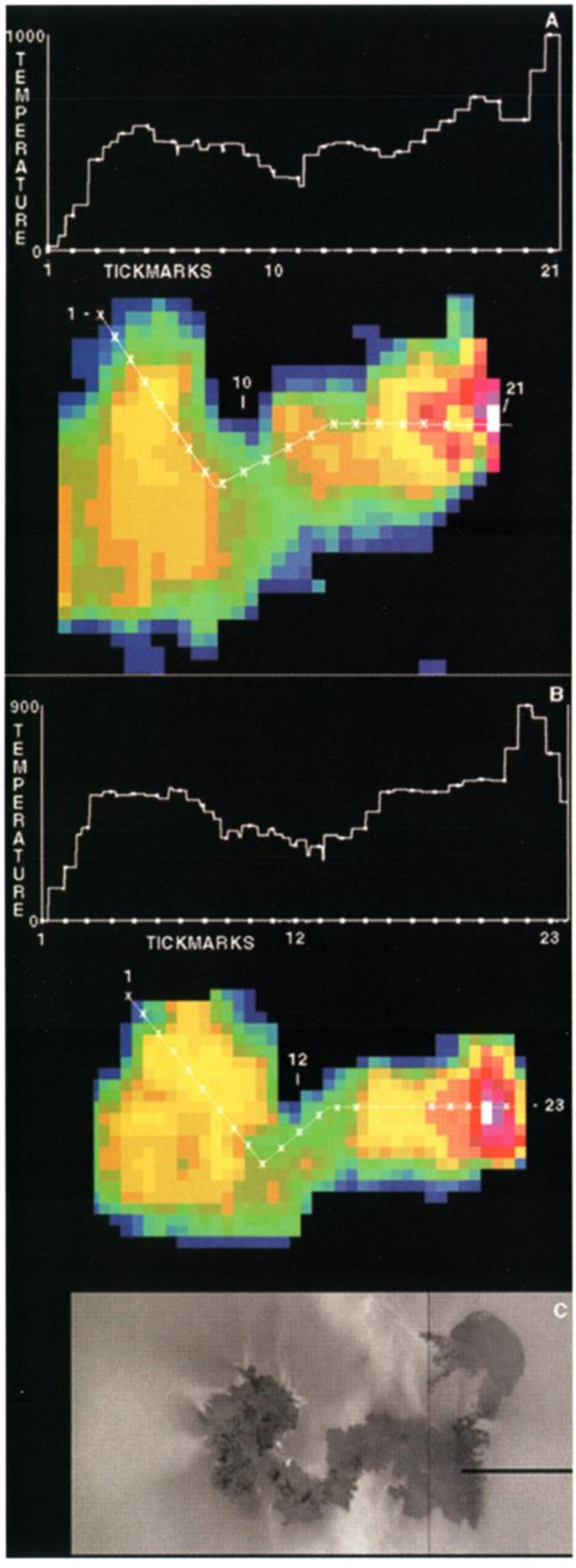

emission to better than ±3° in latitude and longitude. Maui Patera was not imaged by NIMS during the close Io flybys.

The main Amirani flow appears similar to the Prometheus flow field at visible wavelengths, but thermal mapping from NIMS data (Plate 6) shows some significant differences. While Prometheus has a vent area that is significantly hotter than the rest of the flow field, and consistently lower temperatures along the length of the flow, Amirani presents a more complex temperature distribution. Although thermal emission is seen along the whole north-south length of the flow, it is concentrated in a few discrete areas, where temperatures reach up to 1000 K. This is consistent with breakouts of fresh lava along the flow. *Keszthelyi et al.* [this issue] reported changes in the darkest areas on the flow between I24 and I27, which support the interpretation that the hottest areas detected by NIMS correspond to fresh materials breaking out of the flow. The NIMS thermal map is also consistent with the interpretation of *Keszthelyi et al.* [this issue] that the Amirani flow field is similar to a compound flood basalt flow field on Earth, such as the Columbia River Basalts. However, the actual composition cannot be determined from either the morphological analysis or the minimum temperatures obtained from the NIMS data. Our results, as discussed in section 4.2.1 for Prometheus, are consistent with lavas having eruption temperatures either in the basaltic or ultramafic range.

4.3. Hot Spots Showing Low Temperatures: Loki and Emakong

These two hot spots on Io differ from others described in detail in this paper because temperatures above ~400 K were not detected by NIMS at either of these hot spots, even at high spatial resolution. However, in the case of Loki the NIMS observation did not cover the whole caldera and missed the most active area. In the case of Emakong the NIMS observations covered the whole caldera.

The thermal mapping of the Loki caldera was discussed in detail by *Lopes-Gautier et al.* [2000a] from NIMS observations during I24 and by *Spencer et al.* [2000] from observations by the Photopolarimeter Radiometer (PPR) in I24 and I27. Both instruments showed thermal emission from the dark materials on the caldera floor but not from the light colored materials that appear to form an island (or perhaps a raft) inside the caldera. A dark colored crack or valley running through the island showed the highest color temperatures in the NIMS data (350 ± 55 K). Median color temperatures for the dark floor material are 305 ± 44 K; however, NIMS did not image the southern part of the caldera floor, where data from PPR showed the highest floor temperatures (brightness tempera-

Plate 5. (opposite) Prometheus as observed by SSI and NIMS in I24 and I27. (c) Image from SSI, shown for comparison with the NIMS thermal maps from (b) I27 and (a) I24. The NIMS maps represent color temperatures; blues and greens are lowest and yellows and pinks are highest. Both observations show saturation (white) near the hottest (eastern) area and the I24 map is truncated at the left and right edges. Temperature profiles along the flow field are shown for both observations. Profiles show highest temperatures at the eastern part of the flow field, near the inferred vent region. Profiles are consistent with that expected for an insulated flow field. (Note that the pixels at the flow edge, numbered 1, show an artificial zero value which indicates no signal is present.) The lowest temperature that NIMS can detect is 180 K if a pixel is filled.

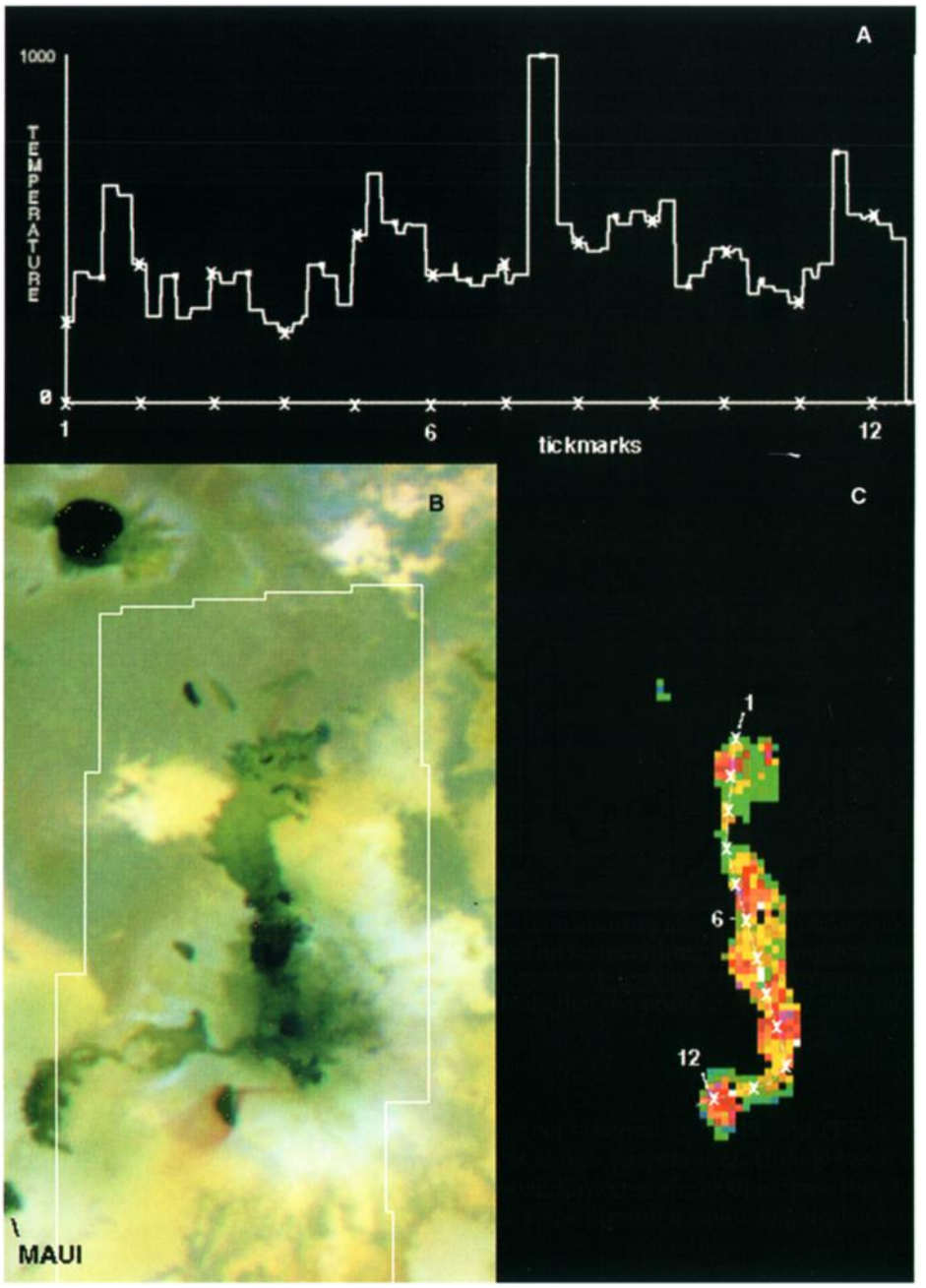

Plate 6. (b) Amirani lava flow field in an image from SSI taken during the C21 orbit. The area observed by NIMS during I27 is delineated. (c) NIMS image showing a map of color temperatures, ranging from purple (lowest) to red (hottest). No thermal emission was detected by NIMS from the flow running west toward Maui. Maui is the dark caldera at the southwestern edge of the SSI image (beyond the edge of the NIMS field of view). Thermal emission was detected from the main Amirani north-south flow, from the Amirani caldera to the south of the main flow, and from an area between the caldera and the main flow that appear to be connected by a fissure surrounded by red deposits. Thermal emission was also detected from a small caldera to the northwest of the main flow that appears dark in the visible image. (a) A temperature profile along the Amirani flow (see numbers on thermal map for locations). Highest temperatures are ~1000 K and are located near the middle of the flow, probably representing a lava breakout. The temperature profile along Amirani has larger variations than that along Prometheus, but both are consistent with insulated flows. Amirani appears to have more breakouts from insulated flows than Prometheus. (Note that the pixels at the flow edge show an artificial zero value which indicates that no signal is present.)

tures from PPR data exceeded 370 K). Earlier analysis of NIMS data from distant observations [*Davies et al.*, 2000b] has measured temperatures up to ~1000 K at Loki. It is possible that similar temperatures were present at Loki during I24, but the hottest areas were not observed by NIMS, and PPR is not sensitive to small areas at high temperatures. Ground-based data [*Howell et al.*, this issue; *Spencer et al.*, 2000] indicate that during I24, Loki was in the early stages of a typical brightening (major eruption).

Both PPR and NIMS data from the flybys are consistent with the Loki caldera being covered by flows of roughly uniform age, or a uniform crust on a lava lake [*Spencer et al.*, 2000]. PPR data obtained during I27 showed changes in thermal emission within the caldera floor, indicating that the hottest (and presumably younger) lavas on the southwest of the caldera in I24 had spread to the west over most of the caldera by I27.

Neither NIMS nor PPR data have been able to distinguish between two possibilities for the eruptive mechanism taking place on Loki: a partly crusted over lava lake or a caldera floor that is being flooded by lava flows. Ground-based data, combined with Galileo data, show that Loki undergoes intermittent brightnenings and suggest two possible scenarios: a lava lake that undergoes periodic overturning or spreading lava flows that are confined by topography [*Rathbun and Spencer*, 2000]. The surface thermal signatures observed by NIMS and PPR are consistent with large expanses of cooling lavas that can fit either the lava lake or the spreading flows scenario.

While Loki has been Io's most often observed hot spot since Voyager, Emakong was not detected as a hot spot until NIMS data from I25 and I27 region observations showed faint thermal emission from the dark caldera. Emakong is located in the center of the Bosphorus Regio region of Io. This region has been repeatedly observed by NIMS prior to the flybys; however, thermal emission from Emakong has never been detected. Emakong was also observed in I24 during our 24INREGION02 observation at 105 km pixel^{-1}, but no thermal emission was detected at this resolution. Unless the NIMS observations consistently missed periods of intense activity, the implication of the lack of detection at low spatial resolution is that thermal emission has remained at a consistently low level. This could imply that activity at Emakong is different from activity at Loki or at other Io hot spots.

NIMS spectra from I24 and I27 show the SO_2 absorption band at 4.1 μm within the same pixels as thermal emission (Figure 2). The Emakong caldera is the only low-albedo location on Io observed at high spatial resolution that shows the SO_2 absorption band. The presence of this band makes it hard to calculate a temperature, as this data point has to be excluded. Using only three bands, data from both I25 and I27 observations are consistent with $T_C \sim 300$ K. When data from the two observations are combined and averaged (to improve signal/noise), we obtain $T_C = 344 \pm 60$ K. These results indicate that the Emakong caldera contains, within the same pixel areas (~25 km^2), cold patches where SO_2 has condensed, as well as volcanically active areas at a minimum temperature of 300 K.

It is unlikely that SO_2 patches would have survived if activity at Emakong had been at high levels recently, with lavas at high temperatures covering large areas of the caldera. A possible scenario for the eruption style at Emakong is a low discharge rate, patchy eruption of silicates in the caldera, with lavas spreading slowly and cooling once they arrive at the surface and covering relatively small areas. Another scenario is that Emakong is the site of sulfur volcanism. *Williams et al.* [this issue] proposed that the bright flows surrounding Emakong may be sulfur flows. If sulfur volcanism is taking place inside the caldera, the temperatures of the active sulfur flows would remain below ~400 K, consistent with what NIMS has observed. The relatively low temperature of sulfur volcanism compared to silicates would allow the surface to approach the SO_2 solidification temperature more quickly and would lower the initial velocity of plumes driven by SO_2. These conditions favor the coexistence of SO_2 and active volcanism within areas of the size of the NIMS pixels relative to silicate volcanism.

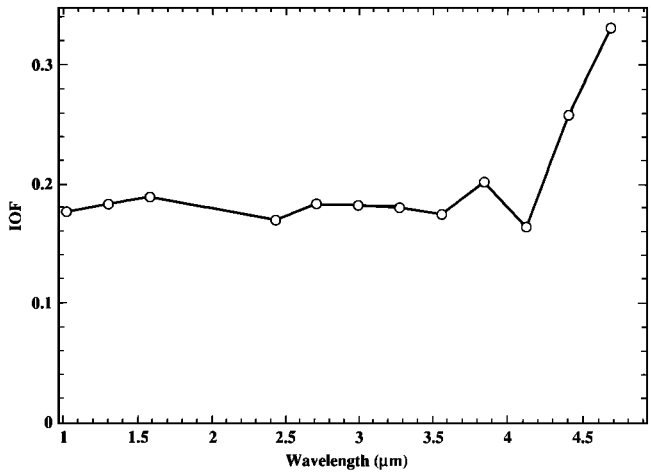

Figure 2. NIMS spectrum (averaged from 12 separate spectra) from inside the Emakong caldera (from 27INREGION01 observation). The low-albedo interior of the Emakong caldera is shown in the SSI image in Plate 4, as is a 4.8-μm map of the NIMS observation. The NIMS spectrum shows thermal emission, consistent with a temperature of ~300 K, within the same pixel as the 4.1-μm SO_2 absorption. Emakong is the only region on Io where patches of SO_2 are seen within the same relatively small areas (~25 km^2) as thermal emission. It is also the only low-albedo region on Io that shows SO_2 absorption in the NIMS data.

4.4. Hot Spots Showing High Temperatures: Pele and Tvashtar

Prior to the flybys, temperatures consistent with ultramafic-type volcanism (>1500 K) had only been obtained for Pillan during a major eruption in 1997 [*McEwen et al.*, 1998b; *Davies et al.*, this issue]. One of the major questions about Io's volcanism is whether high-temperature lavas are present at many or only a few of the hot spots. Since lava cools quickly upon eruption, it is possible that eruption temperatures at any given hot spot are much higher than that measured at a point in time from orbit. In addition, observations having spatial resolution much larger than the sizes of the hot spots make it difficult to detect high temperatures because high temperatures are usually associated with very small areas. Hence, as the pixel size increases, the signal from the hottest components becomes increasingly dominated by that from the cooler components. One of the prime objectives of the flyby observations was to attempt detection of high temperatures at different hot spots. The nighttime observations were particularly suited for measurements of the highest temperatures since two-component fits can be used in the absence of reflected sunlight. Single-temperature determinations for daytime observations (obtained from the longer wavelengths in the NIMS range) tend to be dominated by the lower temperatures that cover larger areas within the pixels.

4.4.1. Pele. NIMS obtained a nighttime observation of Pele in I27. A brightness temperature map (Plate 7) at 1 μm showed that very high temperatures are present in a broad band across the southern half of the caldera, particularly in the southeast corner. In the corner where the highest temperatures

are suspected, all wavelengths longer than 1 μm are saturated, so precise determination of the highest temperatures cannot be made. We also excluded pixels where the signal at 1 μm is too low to be significantly above the noise level. The remaining pixels fall into a region adjacent to the saturated area referred to above. These pixels are shown in Plate 8. The spectra from these pixels were used to determine the highest temperatures that NIMS could measure from this observation.

We used the Planck function to obtain two-temperature fits to these individual spectra. This was done because (1) the spectra could be better fitted by two temperatures rather than a single temperature and (2) previous work using distant observations of Pele [*Davies et al.*, this issue] indicates that the spectra are better fitted by two components. The two-component fits were performed using

$$f_1 B(\lambda, T_1) + f_2 B(\lambda, T_2) = I(\lambda), \quad (4)$$

where λ is wavelength, f_1 and f_2 are the fractional areas of the two components, and T_1 and T_2 are their temperatures, $B(\lambda, T)$ is Planck function and $I(\lambda)$ is the observed intensity. The fit was performed using the method of simulated annealing [*Metropolis et al.*, 1953; *Press et al.*, 1986].

Figure 3 shows spectra where NIMS is moving slowly over a small region of very high temperatures. The two-component fit gave reasonable determination of temperatures for 15 separate spectra which are all overlapping. Three examples of fits to individual spectra are shown in Figure 3. Although there are only six points in each spectrum (because of saturation of middle wavelengths) the consistency of the temperatures and of the overall shapes of the spectra increase confidence in the results. We derived a median temperature for the hot component of $T_1 = 1760 \pm 210$ K. This range implies that the Pele caldera has small areas where the lavas are at temperatures consistent with ultramafic compositions. This temperature range for Pele overlaps with the range of 1440 ± 150 K proposed by *Zolotov and Fegley* [2000] on the basis of sulfur and oxygen fugacities in the Pele plume from HST data obtained in 1996.

4.4.2. Tvashtar. This chain of calderas was observed by NIMS and SSI in I25 and I27. Fortuitously, during orbit I25, Io was observed from the ground almost simultaneously with the Galileo observations [*Howell et al.*, this issue; D. S. Acton et al., unpublished manuscript, 2000]. Both ground-based and Galileo observations revealed a region of very high temperatures that caused pixels in SSI observations to bleed [*McEwen et al.*, 2000] and pixels in the NIMS observations to saturate. The ground-based and SSI observations were interpreted as images of a fire fountain erupting hot lavas [*McEwen et al.*, 2000]. Temperatures estimated from the ground-based observations ranged from 1300 to 1900 K (D. S. Acton et al., unpublished manuscript, 2000). The observation by NIMS taken in I25 (25INGIANTS01) covers the eastern part of the active caldera, and the pixels at most wavelengths are saturated. The highest temperature derived from a single-component fit (using a non-saturated pixel) yielded $T_C = 1060 \pm 60$ K (area of 0.003 km^2). This estimate is a lower limit on the eruption temperature for two reasons. First, it was derived from a pixel that is most likely cooler than the hottest pixel in the observation (the pixel over the hottest area observed by SSI showed saturation at most wavelengths in the NIMS observation). Second, the observation was taken in daytime, and the single-component fit to the longer wavelengths will not be representative of small areas having high temperatures and thus will underestimate the highest temperature within the pixel. The NIMS-derived temperature is consistent with the range reported from ground-based observations, which imply that lavas may be ultramafic in composition.

Data returned from I27 show that activity in the region observed had fallen to a lower level by February 2000. NIMS pixels from the same and adjacent locations as in I25 do not show saturation and yield one-component temperature fits between 500 and 600 K.

5. Implications for Io's Volcanism

The Pillan eruption of 1997 gave the first indication that very high temperatures, consistent with ultramafic volcanism, are present on Io [*McEwen et al.*, 1998b]. One question that arose from the Pillan eruption was whether this volcano was unique in terms of showing temperatures consistent with ultramafic lavas or whether these lavas are common on Io and simply not normally observed. Temperatures derived from remote-sensing observations have to be considered minimum temperatures as magma cools quickly once it reaches the surface [e.g., *Flynn and Mouginis-Mark*, 1992]. Pillan's 1997 eruption was unusual because it had a sufficiently high mass eruption rate to cover relatively large areas on the surface with high-temperature lavas, which could be detected from distant observations. It was fortuitous that Galileo was able to observe the eruption while the mass eruption rate was high. Activity at Pillan has been observed as early as Galileo's orbit G2 [*Lopes-Gautier et al.*, 1999], but temperatures indicating clearly ultramafic compositions could not be measured for orbits other than C9 (June 1997) [*Davies et al.*, this issue].

McEwen et al. [1998b] first proposed the Pillan lavas to be ultramafic on the basis of temperature determinations of up to 1825 K. Terrestrial basalts typically erupt at 1300 K to 1450 K [*Morse*, 1980], while terrestrial ultramafic lavas (komatiites) were erupted between 1700 K and 1900 K [*Hess*, 1989; *Herzberg*, 1992]. The NIMS I27 data detected high temperatures at Pele that are consistent with ultramafic volcanism. Although superheated basalts are also a possibility, we agree with the discussion presented by *McEwen et al.* [1998b] that ultramafic composition is a more feasible explanation for Io lava temperatures on Io.

Pele and Pillan may not be unique. It is feasible that such high temperatures are common, but as yet undetected, on Io. Higher-resolution observations by NIMS have increased detection of small areas at high temperatures, though none of the temperature determinations reported here (except for Pele) demand ultramafic compositions. However, the bulk of the flyby data consisted of daytime observations. Nighttime observations, such as that of Pele in I27 by NIMS, are the most suitable for determination of high temperatures, as signal in the short wavelengths in the NIMS range contains only thermal emission and no reflected sunlight. Most of the hot spots observed during the Galileo flybys were in sunlight. In these cases, the estimated temperatures (up to ~1000 K) were obtained only using the longer wavelengths in the NIMS range, which are dominated by emission from regions at lower temperatures which are typically orders of magnitude larger in area than the highest temperature regions. Therefore temperatures determined from daytime NIMS observations provide only a minimum magma temperature estimate, and our results do not rule out ultramafic compositions for Prometheus, Amirani, Tvashtar, and other hot spots.

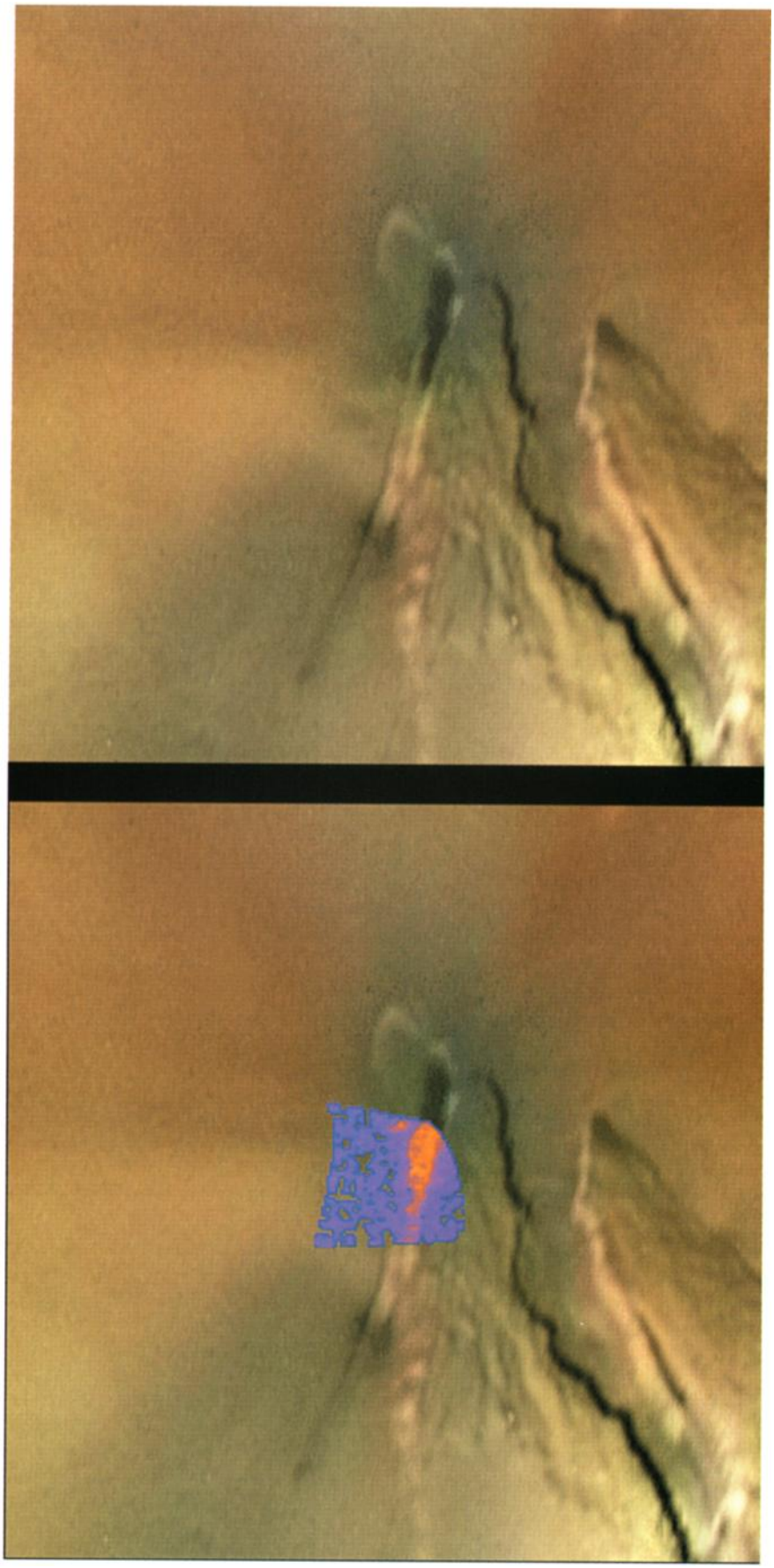

Plate 7. Pele was observed by NIMS during I27. (right) Image obtained by the Voyager spacecraft in 1979, which is still the highest-resolution daytime image available of this area. (left) A brightness temperature map made from the NIMS observation, superimposed on the Voyager image. This shows that the highest temperatures are located in a broad band across the southern part of the caldera. The Voyager context image is 200 km across. The coregistration between the NIMS data and the Voyager image is not precise because of uncertainties in the Voyager pointing and the lack of visible features in the nighttime NIMS observation. Errors up to half the size of the NIMS data area are possible.

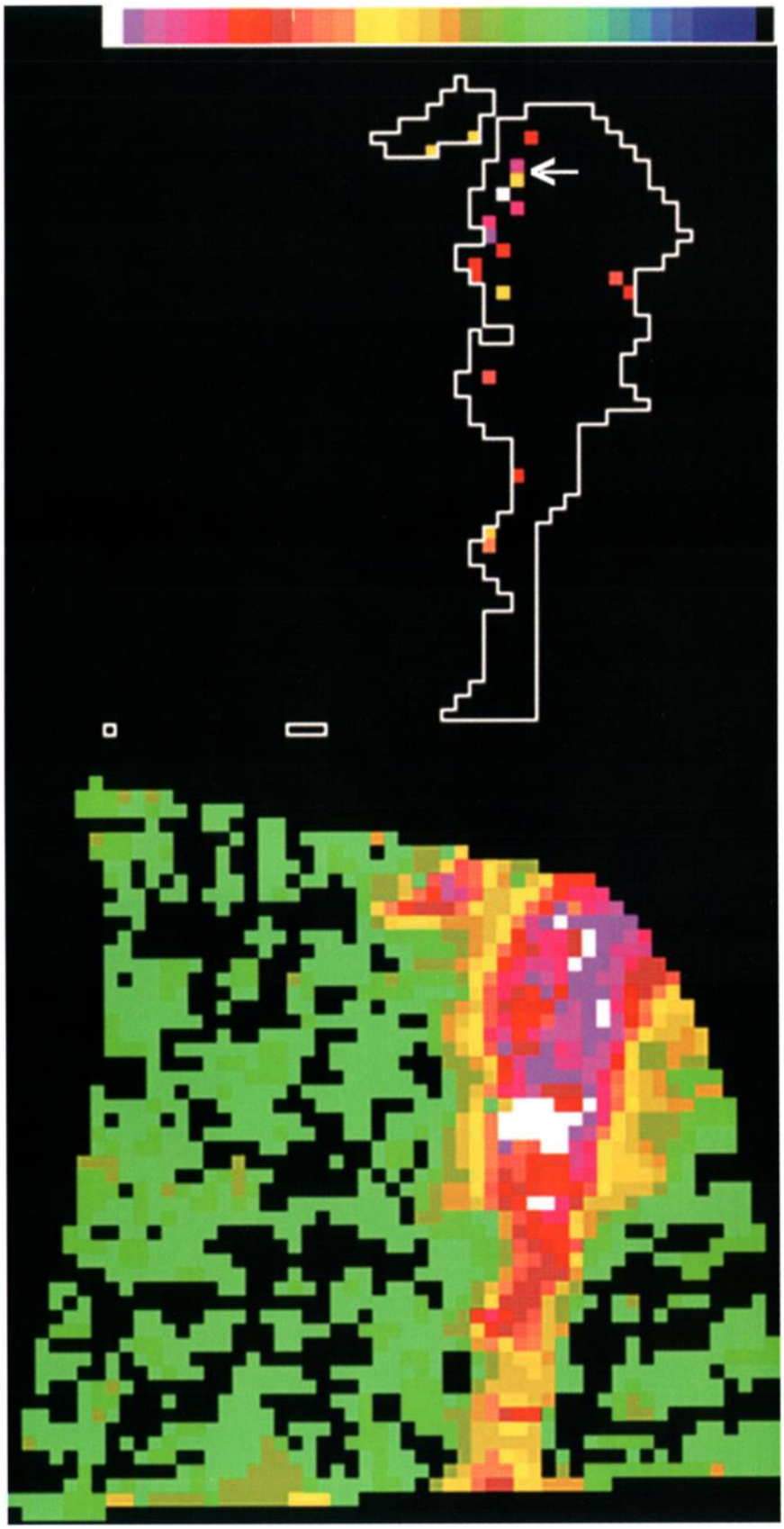

Plate 8. NIMS temperature maps made from the Pele observation obtained during I27 (compare with Plate 7). (left) Brightness temperature map at 1.3 μm. Black areas (inside the observation, not beyond borders) and green areas have signal too low to be distinguished from noise. Areas that are dark red, pink, magenta, and white (see color bar) are saturated at wavelengths beyond 1.3 μm, so cannot be used to determine color temperature (T_C). The nominal brightness temperatures (at 1.3 μm) are approximately yellow (590 K), red (640 K), and white (700 K). (right) Color temperature map. For reference, we show an outline of the hottest areas where the radiances at 1.3 μm have a signal significantly above the noise level. We also show pixels for which color temperatures could be obtained (ranging from yellow, 1500 K, to red, 2200 K). The arrow points to the location where a cluster of individual spectra were used to determine the highest reliable temperatures at Pele (1760 $\pm$ 210 K). Note that higher color temperatures may be present in the hottest areas, but the saturation at longer wavelengths than 1.3 μm prevents us from determining reliable color temperatures.

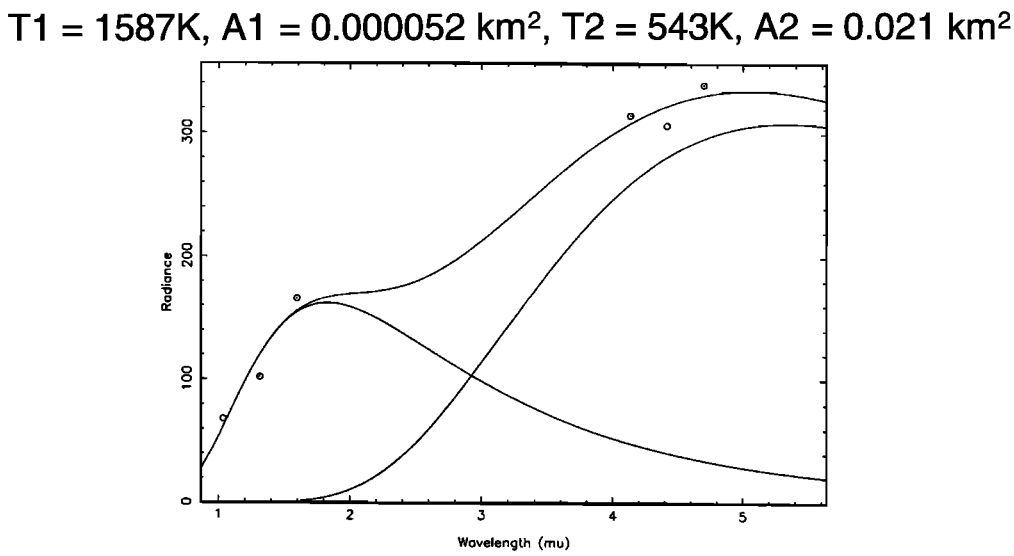

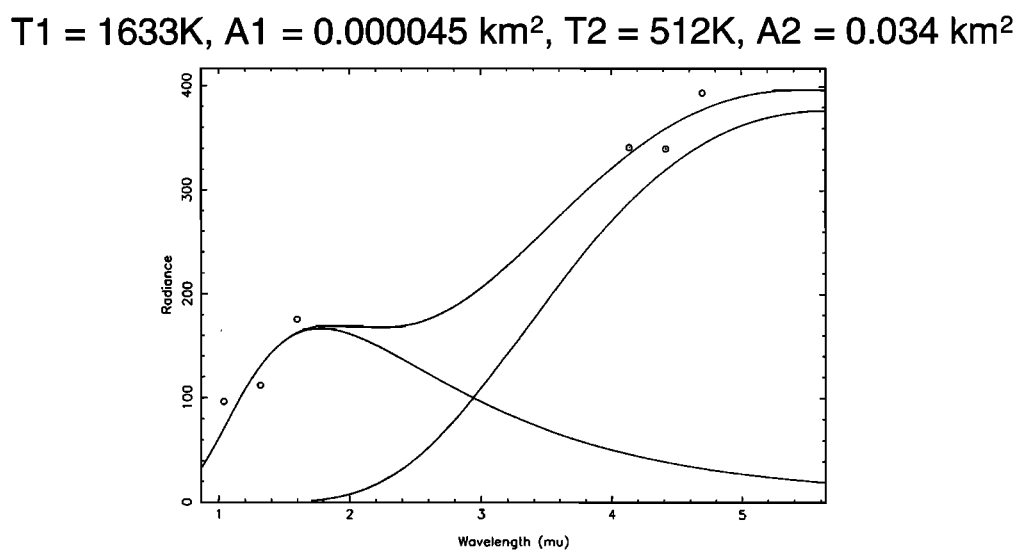

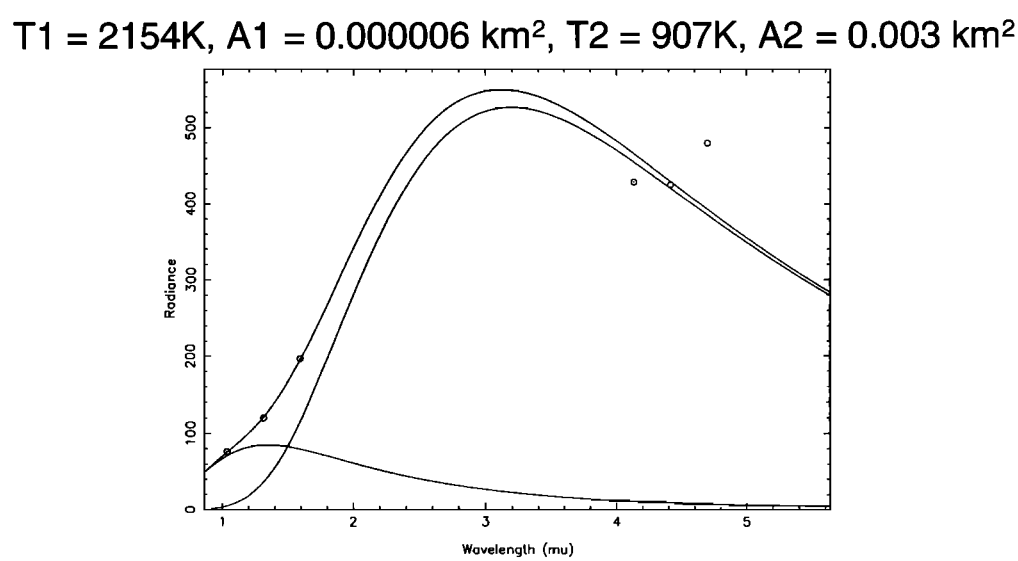

Figure 3. Typical examples of two component fits to NIMS spectra of Pele. Two-component fits were done to 15 NIMS spectra from the same region which all overlapped in areal coverage. The middle wavelengths were saturated in all the spectra. The median hot component derived from the 15 spectra yielded T_1 = 1760 ± 210 K.

Our results rule out low-temperature volcanism (such as sulfur) for most of the observed hot spots but generally represent minimum temperature measurements because of effects of cooling rates and spatial resolution. We set no upper limits on temperature of small exposed areas within the observed hot spots nor temperatures within crusted lava lakes or tube-fed flows, where most of the exposed surface can consist of cooling lavas that are several hundred degrees cooler than eruption temperatures. Moreover, if the eruption has temporarily halted during the time of the observation, high temperatures would not be present and only temperatures consistent with those of cooling lavas would be detected. It is therefore not yet possible to infer differences in magma temperature or composition for various hot spots from the available temperature data that we have for Io, though such inferences may be valid on the basis of morphological data or unusual characteristics. One example is the interior of the Emakong caldera, where low thermal emission combined with the presence of SO_2 in a volcanically active region support the conclusions of *Williams et al.* [this issue] that Emakong and its surroundings may be a site of sulfur volcanism. So far, Emakong is unique among Io's hot spots as the only location where NIMS has detected SO_2 and thermal emission within the same pixel (~20–25 km^2). It is unclear whether Emakong is a unique hot spot in this respect. NIMS has only observed ~5% of Io's surface at resolutions better than ~25 km/NIMS pixel, and it is possible that thermal emission at levels similar to that at Emakong have not been so far detected.

The three flybys in 1999 and 2000 covered only a very limited area of Io's surface and mostly of persistently active volcanic regions at low latitudes on the anti-Jovian hemisphere. To obtain a representative sample of the thermal behavior over the whole of Io, additional observations need to be made, including regional observations of areas at high latitudes and on the Jupiter-facing hemisphere to help to determine the overall distribution of hot spots on the surface. What we have learned from the high-resolution NIMS data includes that (1) the number of individual hot spots observed increased by a factor of ~3 with increased spatial resolution of a factor of about 10; (2) some previously known hot spots have complex structures or consist of several individual volcanic centers; (3) Prometheus, Amirani, and Tvashtar show temperatures higher than 1000 K that are consistent with either basaltic or ultramafic volcanism; (4) temperatures detected at Pele are consistent with ultramafic volcanism; (5) Emakong provides a so-far unique example of coexistence of SO_2 and thermal emission within 25 km^2; (6) SO_2 deposits at Amirani, Prometheus, and Culann show that white areas at visible wavelengths do not coincide with highest concentrations of SO_2; and (7) a small nonactive caldera near Chaac has very high visible albedo and the highest SO_2 concentration so far detected by NIMS; the shape of the SO_2 deposit appears to be controlled by the topography of the caldera, suggesting emplacement by flow mechanism.

Acknowledgments. We thank John Spencer and Karl Hibbitts for detailed and helpful reviews of the manuscript, Jason Perry for his help in gathering data for Table 2, and the Galileo flight team for their dedication to making the Io flybys a success. The research described in this paper was carried out at the Jet Propulsion Laboratory, California Institute of Technology, under a contract with the National Aeronautics and Space Administration.

References

Carlson, R. W., P. R. Weissman, W. D. Smythe, J. C. Mahoney, and the NIMS Science and Engineering Teams, Near-Infrared Spectrometer Experiment on Galileo, *Space Sci. Rev.*, *60*, 457–502, 1992.

Carlson, R. W., et al., The distribution of sulfur dioxide and other infrared absorbers on the surface of Io in 1997, *Geophys. Res. Lett.*, *24*, 2479–2482, 1997.

Carlson, R. W., et al., Radiolytic influence on the surface composition of the Galilean satellites, paper presented at Jupiter: Planet, Satellites, and Magnetosphere Conference, Lab. for Atmos. and Space Phys., Univ. of Colo., Boulder, Colo., June 25–30, 2001.

Carr, M. H., A. S. McEwen, K. A. Howard, F. C. Chuang, P. Thomas, P. Schuster, J. Oberst, G. Neukum, G. Schubert, and the Galileo Imaging Team, Mountains and calderas on Io: Possible implications for lithospheric structure and magma generation, *Icarus*, *135*, 146–165, 1998.

Crisp, J., and S. Baloga, A model for lava flows with two thermal components, *J. Geophys. Res.*, *95*, 1255–1270, 1990.

Davies, A. G., A. S. McEwen, R. Lopes-Gautier, L. Keszthelyi, R. W. Carlson, and W. D. Smythe, Temperature and area constraints of the South Volund volcano on Io from the NIMS and SSI instruments during the Galileo G1 orbit, *Geophys. Res. Lett.*, *24*, 2447–2450, 1997.

Davies, A. G., R. Lopes-Gautier, W. D. Smythe, and R. W. Carlson, Silicate cooling model fits to Galileo NIMS data of volcanism on Io, *Icarus*, *148*, 211–225, 2000a.

Davies, A. G., L. P. Keszthelyi, R. Lopes-Gautier, W. D. Smythe, L. Kamp, R. W. Carlson, and the Galileo NIMS and SSI Teams, Eruption evolution of major volcanoes on Io: Galileo takes a close look, Lunar Planet. Sci. Conf. [CD-ROM], XXXI, Abstract 1754, 2000b.

Davies, A. G., L. P. Keszthelyi, D. A. Williams, C. B. Phillips, A. S. McEwen, R. Lopes-Gautier, W. D. Smythe, L. W. Kamp, L. A. Soderblom, and R. W. Carlson, Thermal signature, eruption style, and eruption evolution at Pele and Pillan on Io, *J. Geophys. Res.*, this issue.

Douté, S., R. Lopes-Gautier, W. D. Smythe, L. W. Kamp, R. Carlson, and the Galileo NIMS Team, Dynamics and evolution of SO_2 gas condensation around Prometheus-like volcanic plumes on Io as seen by the Near-Infrared Mapping Spectrometer on Galileo, paper presented at American Astronomical Society Division for Planetary Sciences Meeting, Pasadena, Calif., 2000.

Douté, S., B. Schmitt, R. Lopes-Gautier, R. Carlson, L. Soderblom, J. Shirley, and the Galileo NIMS Team, Mapping the SO_2 frost on Io by the modeling of NIMS hyperspectral images, *Icarus*, *149*, 107–132, 2001a.

Douté, S., et al., Spatial distribution and chemical nature of the 1 micron absorber on Io's surface inferred by the Near-Infrared Mapping Spectrometer and the solid-state imager on Galileo, paper presented at Jupiter: Planet, Satellites, and Magnetosphere Conference, Lab. for Atmos. and Space Phys., Univ. of Colo., Boulder, Colo., June 25–30, 2001b.

Fanale, F. P., T. V. Johnson, and D. L. Matson, Io: A surface evaporite deposit?, *Science*, *186*, 922–925, 1974.

Flynn, L. P., and P. J. Mouginis-Mark, Cooling rate of an active Hawaiian flow from nighttime spectroradiometer measurements, *Geophys. Res. Lett.*, *19*, 1783–1786, 1992.

Geissler, P. E., A. S. McEwen, L. Keszthelyi, R. Lopes-Gautier, J. Granahan, and D. P. Simonelli, Global color variations on Io, *Icarus*, *140*, 265–281, 1999.

Geissler, P. E., A. S. McEwen, C. Phillips, D. Simonelli, R. Lopes-Gautier, and S. Douté, Galileo imaging of SO_2 frosts on Io, *J. Geophys. Res.*, this issue.

Goguen, J. D., et al., Io's hot spots: Infrared photometry of satellite occultations, *Icarus*, *76*, 465–484, 1988.

Goguen, J. D., A. Lubenow, and A. Storrs, HST NICMOS images of Io in Jupiter's shadow, *Bull. Am. Astron. Assoc.*, *30*, 1120, 1998.

Herzberg, C., Depth and degree of melting of komatiites, *J. Geophys. Res.*, *97*, 4521–4540, 1992.

Hess, P. C., *Origins of Igneous Rocks*, Harvard Univ. Press, Cambridge, Mass., 1989.

Howell, R. R., et al., Ground-based observations of volcanism on Io in 1999 and early 2000, *J. Geophys. Res.*, this issue.

Kargel, J. S., P. Delmelle, and D. B. Nash, Volcanogenic sulfur on Earth and Io: Composition and spectroscopy, *Icarus*, *142*, 249–280, 1999.

Keszthelyi, L., et al., Imaging of volcanic activity on Jupiter's moon Io

by Galileo during Galileo Europa mission and Galileo millennium mission, *J. Geophys. Res.*, this issue.

Kieffer, S. W., R. Lopes-Gautier, A. S. McEwen, W. Smythe, L. Keszthelyi, and R. Carlson, Prometheus: Io's wandering plume, *Science*, *288*, 1204–1208, 2000.

Lopes-Gautier, R., Volcanism on Io, in *Encyclopedia of Volcanoes*, edited by H. Sigurdsson et al., pp. 709–726, Academic, San Diego, Calif., 1999.

Lopes-Gautier, R., A. G. Davies, R. W. Carlson, W. D. Smythe, L. Kamp, L. A. Soderblom, F. E. Leader, R. Mehlman, and the Galileo NIMS Team, Hot spots on Io: Initial results from Galileo's Near-Infrared Mapping Spectrometer, *Geophys. Res. Lett.*, *24*, 2439–2442, 1997.

Lopes-Gautier, R., et al., Hot spots on Io: Global distribution and variations in activity, *Icarus*, *140*, 243–264, 1999.

Lopes-Gautier, R. M. C., et al., A close-up look at Io from Galileo's Near-Infrared Mapping Spectrometer, *Science*, *288*, 1201–1204, 2000a.

Lopes-Gautier, R., et al., Galileo at Io: New results from the Near-Infrared Mapping Spectrometer, *Eos Trans. AGU*, *81*(48), Fall Meet. Suppl., F788, 2000b.

Marchis, F. R. Prangé, and J.-C. Christou, Adaptive optics mapping Io's volcanism in the thermal IR (3.8 microns), *Icarus*, *148*, 384–396, 2000.

Marchis, F. R. Prangé, and T. Fusco, A survey of Io's volcanism by adaptive optics observations in the 3.8 μm thermal band (1996–1999), *J. Geophys. Res.*, this issue.

McEwen, A. S., D. P. Simonelli, D. R. Senske, K. P. Klaasen, L. Keszthelyi, T. V. Johnson, P. E. Geissler, M. H. Carr, and M. J. S. Belton, High-temperature hot spots on Io as seen by the Galileo solid-state imaging (SSI) experiment, *Geophys. Res. Lett.*, *24*, 2443–2446, 1997.

McEwen, A. S., et al., Active volcanism on Io as seen by Galileo SSI, *Icarus*, *135*, 181–219, 1998a.

McEwen, A. S., et al., High-temperature silicate volcanism on Jupiter's moon Io, *Science*, *281*, 87–90, 1998b.

McEwen, A. S., et al., Galileo at Io: Results from high-resolution imaging, *Science*, *288*, 1193–1198, 2000.

Milazzo, M. P., L. P. Keszthelyi, and A. S. McEwen, Observations and initial modeling of lava-SO_2 interactions at Prometheus, Io, *J. Geophys. Res.*, this issue.

Morse, S. A., *Basalts and Phase Diagrams*, Springer-Verlag, New York, 1980.

Pearl, J., and W. M. Sinton, Hot spots on Io, in *Satellites of Jupiter*, edited by D. Morrison, pp. 724–755, Univ. of Ariz. Press, Tucson, 1982.

Press, W. H., B. P. Flannery, S. A. Teukolsky, and W. T. Vetterling, *Numerical Recipes*, pp. 326–334, Cambridge Univ. Press, New York, 1986.

Radebaugh, J., L. P. Keszthelyi, A. S. McEwen, E. P. Turtle, W. Jaeger, M. Milazzo, and the Galileo Team, Paterae on Io: A new type of volcanic caldera?, *J. Geophys. Res.*, this issue.

Rathbun, J. A., and J. R. Spencer, Loki: History of eruptions from groundbased and Galileo data, *Eos Trans. AGU*, *81*(48), Fall Meet. Suppl., F794, 2000.

Schenck, P., and H. Hargitai, Morphology and distribution of mountains on Io, *Bull. Am. Astron. Soc.*, *30*(3), 1121, 1998.

Smythe, W. D., et al., Galilean satellite observation plans for the Near-Infrared Mapping Spectrometer on the Galileo spacecraft, *J. Geophys. Res.*, *100*, 18,957–18,972, 1995.

Smythe, W. D., R. Lopes-Gautier, S. Douté, S. W. Kieffer, R. W. Carlson, L. Kamp, and F. E. Leader, Evidence for massive sulfur dioxide deposit on Io, *Bull. Am. Astron. Soc.*, *32*(3), 1047–1048, 2000.

Soderblom, L. A., K. J. Becker, T. L. Becker, R. W. Carlson, A. G. Davies, J. S. Kargel, R. L. Kirk, R. Lopes-Gautier, W. D. Smythe, and J. M. Torson, Deconvolution of Galileo NIMS-day-side spectra of Io into thermal, SO_2, and non-SO_2 components, *Lunar Planet. Sci. Conf.* [CD-ROM], *XXX*, Abstract 1901, 1999.

Spencer, J. R., A. S. McEwen, M. A. McGarth, P. Sartoretti, D. B. Nash, K. S. Noll, and D. Gilmore, Volcanic resurfacing of Io: Post-repair HST imaging, *Icarus*, *127*, 221–237, 1997.

Spencer, J. R., J. A. Rathbun, L. D. Travis, L. K. Tamppari, L. Barnard, T. Z. Martin, and A. S. McEwen, Io's thermal emission from the Galileo Photopolarimeter-Radiometer, *Science*, *288*, 1198–1201, 2000.

Veeder, G. J., D. L. Matson, T. V. Johnson, D. L. Blaney, and J. D. Goguen, Io's heat flow and infrared radiometry: 1983–1993, *J. Geophys. Res.*, *99*, 17,095–17,162, 1994.

Williams, D. A., R. Greeley, R. Lopes-Gautier, and A. G. Davies, Evaluation of sulfur flow emplacement on Io from Galileo data and numerical modeling, *J. Geophys. Res.*, this issue.

Zolotov, M. Y., and B. Fegley, Eruption conditions of Pele volcano on Io inferred from chemistry of its volcanic plume, *Geophys. Res. Lett.*, *27*, 2789–2792, 2000.

E. Barbinis, R. W. Carlson, A. G. Davies, L. W. Kamp, R. M. C. Lopes, M. Segura, J. Shirley, and W. D. Smythe, Jet Propulsion Laboratory, California Institute of Technology, MS 183-601, 4800 Oak Grove Drive, Pasadena, CA 91109. (rcarlson@lively.jpl.nasa.gov; Ashley.Davies@jpl.nasa.gov; lkamp@jpl.nasa.gov; rlopes@lively.jpl.nasa.gov; wsmythe@jpl.nasa.gov)

S. Douté, CNRS Laboratoire de Planetologie de Grenoble, Bat D de Physique BP 53, F-38041 Grenoble Cedex 9, France. (Sylvain.Doute@planeto.obs.ujf-grenoble.fr)

P. E. Geissler and A. S. McEwen, Lunar and Planetary Laboratory, University of Arizona, Tucson, AZ 85721. (mcewen@pirl.lpl.arizona.edu)

S. W. Kieffer, S. W. Kieffer Science Consulting, Inc., P.O. Box 520, Bolton, Ontario, Canada L7E 5T4. (skieffer@geyser.com)

F. Leader and R. Mehlman, IGPP, University of California, Los Angeles, CA 90095.

L. A. Soderblom, U.S. Geological Survey, 2255 North Gemini Drive, Flagstaff, AZ 86001. (lsoderblom@usgs.gov)

(Received January 31, 2001; revised August 1, 2001;
accepted August 3, 2001.)